9-12-2019

Target Detection in Heterogeneous Clutter with Low Resolution Radar

Kyle G. Stankowski

TARGET DETECTION IN HETEROGENEOUS CLUTTER WITH LOW RESOLUTION RADAR

THESIS

Kyle G. Stankowski

AFIT-ENG-MS-19-S-011

DEPARTMENT OF THE AIR FORCE
AIR UNIVERSITY

AIR FORCE INSTITUTE OF TECHNOLOGY

Wright-Patterson Air Force Base, Ohio

AFIT-ENG-MS-19-S-011

TARGET DETECTION IN HETEROGENEOUS CLUTTER WITH LOW RESOLUTION RADAR

THESIS

Presented to the Faculty

Department of Electrical and Computer Engineering

Graduate School of Engineering and Management

Air Force Institute of Technology

Air University

Air Education and Training Command

in Partial Fulfillment of the Requirements for the

Degree of Master of Science in Electrical Engineering

Kyle G. Stankowski, B.S.E.E.

12 September 2019

AFIT-ENG-MS-19-S-011

TARGET DETECTION IN HETEROGENEOUS CLUTTER WITH LOW RESOLUTION RADAR

THESIS

Kyle G. Stankowski, B.S.E.E.

Committee Membership:

Dr. Julie Jackson
Chairman

Dr. Richard Martin
Member

Dr. Peter Collins
Member

Abstract

This thesis develops a framework for SAR target detection and super-resolution in low-resolution environments. The primary focus in this research is the background clutter heterogeneity that often accompanies low range and cross-range resolutions.

A clutter replacement model is used for the target to account for areas of background clutter which are obstructed by a target and do not have a reflective path from the transmitter to the receiver. This thesis develops a corrective model to define the detection and false alarm rates of the detector more accurately than a traditional model in which the radar return from the target supplements the existing clutter. An in-depth study is conducted on a scenario with a specific set of conditions, then the parameters are modified to observe their effects.

The super-resolution model reduces the amount of positioning error that occurs in a wide resolution cell. If a target is smaller than the resolution cell, it is typically assumed to be at the center of the cell; this estimation is made to reduce the amount of error between the true and estimated positions. In a heterogeneous clutter cell, the clutter replacement model leverages the different scattering distributions among the individual clutter types to generate a probability distribution function for the proportions of each clutter type which are replaced by a target. The location of the target can be extrapolated from the clutter replacement areas, and a multiple hypothesis detection test is conducted to determine which location estimate yields the lowest average error.

Acknowledgements

I would like to take this opportunity to thank everyone at NASIC who helped me learn about the opportunities available at AFIT and accommodated my work schedule to allow me to pursue my degree.

Thank you to the AFIT faculty for always having an open door and being willing to answer any questions. Special thanks go out to Maj JR Lievsay and my advisor, Dr. Julie Jackson, for getting me started on this path of study and teaching me so much about the world of academic research. Thank you to my other committee members, Dr. Peter Collins and Dr. Richard Martin, for their time in reviewing this document.

Thank you to my peer network of support, my fellow RAIL students - as tangential as some of our discussions may have become, they always left me with some new thoughts on how to approach problems differently and improve my research. Lastly, thank you to my family and friends for scheduling "life" around my schooling and providing a constant stream of positivity.

Kyle G. Stankowski

Table of Contents

Page

Page

List of Figures

List of Tables

List of Abbreviations

AWGN	additive white Gaussian noise
CDF	cumulative distribution function
CLT	central limit theorem
DAB	Digital Audio Broadcast
DVB	Digital Video Broadcast
FFT	fast Fourier transform
i.i.d.	independent, identically-distributed
LRT	likelihood ratio test
LTE	Long-Term Evolution
MLE	maximum likelihood estimate
PDF	probability distribution function
PMF	probability mass function
PRF	pulse repetition frequency
RCS	radar cross-section
RF	radio frequency
ROC	receiver operating characteristic
SAR	synthetic aperture radar
SIRV	spherically-invariate random variable
SLAR	side-looking airborne radar
SNR	signal-to-noise ratio

List of Symbols

Symbol		Page
$\mathcal{R}$	risk	19
C_{ij}	cost for multiple hypothesis detection scheme	19
Y	number of target positions in multiple hypothesis detection scheme	19
θ_s	sub-aperture azimuth support	21
m	total number of pulses collected	24
N	number of sub-apertures	24
v	aircraft velocity	24
R	one-way radar range	24
f_{PRF}	pulse repetition frequency	24
S_r	received radar return	25
$W(a_k, b_k)$	realization from a complex Weibull-distributed random variable with scale and shape parameters specific to the k^{th} clutter patch	25
ϵ_k	area of clutter patch k reduced by a target or its shadow	26
R	radar range	28
Z	radar altitude	28
$\ell_{CR}(\phi)$	target cross-range length as viewed from receiver	28
V	complex additive white Gaussian noise	30
I	the real-valued (in-phase) component of S_r	32
Q	the imaginary (quadrature) component of S_r	32
σ_0^2	I-component clutter variance (no target)	32
σ_1^2	I-component variance of resolution cell containing clutter and target	33
λ	likelihood threshold	34
σ_{ck}^2	variance of the real component of the k^{th} clutter patch	36

Symbol		Page
σ_t^2	variance of the real component of the target return	36
P_{fa}	probability of false alarm	36
P_d	probability of detection	36
Γ_1	detection region for H_1	37
Γ_F	Gamma function	37
γ_f	Lower incomplete gamma function	37
ν	χ^2 degrees of freedom	37
γ	detection threshold	39
Γ_0	detection region for H_0	39
$\mathcal{R}$	risk for multiple hypothesis detection scheme	45
C_{ij}	cost for choosing H_i when H_j is true in a multiple hypothesis detection scheme	45
$u(i)$	index of σ_{1i}^2 among the sorted σ_1^2 values for all hypotheses	46
ℓ_R	length of the target in the range dimension	48
ℓ_{CR}	length of the target in the cross-range dimension	48
D	binary detection indicator of the resolution cell	60
J	number of Monte Carlo simulation trials	61
p_d	simulated probability of detection	61
p_{fa}	simulated probability of false alarm	61
T	binary target indicator of the resolution cell	61
F_A	number of false alarms in an simulation	63
A_{ov}	area of vertical target overlay onto 2-D grid	74

TARGET DETECTION IN HETEROGENEOUS CLUTTER WITH LOW RESOLUTION RADAR

I. Introduction

In synthetic aperture radar (SAR) applications, low range resolution is a consequence of poor signal bandwidth. This can arise from using inexpensive radar hardware or utilizing signals of opportunity which are not designed to maximize bandwidth. This research focuses on monostatic or pseudo-monostatic scenarios in which signal bandwidth is low, resulting in wide resolution cells.

Land cover maps are often available from the United States Geographical Survey to determine the background composition at specific locations where a synthetic aperture radar (SAR) system is collecting imagery [1]; however, more sophisticated models must be created to account for circumstances in which coarse resolution cells contain heterogeneous clutter. Additionally, a portion of the clutter may be concealed by the target of interest and is therefore not received. Traditional methods of radar detection, which are often used for finer-resolution scenarios, can be inaccurate under these conditions.

A typical SAR detection model, as used in [2], [3], and [4], relies on a set of hypotheses which compares the distribution of the background clutter against the distribution of a target of interest. The key assumption is that the target comprises the entire resolution cell. For large cells, this is rarely the case, and a degree of model mismatch exists which causes the detector to miss targets and record false-alarms at higher-than-expected rates [5].

This thesis examines the statistical properties of large resolution cells which con-

tain heterogeneous clutter. The hybrid clutter background is calculated in conjunction with the prior probability for the position of a target of interest to determine the overall scattering statistics of a target-present resolution cell, in order to develop a detection methodology. A location estimator is implemented to lessen the degree of range and cross-range ambiguities associated with large resolution cells.

Methods developed in this thesis are a crucial component to assuring the success of low-cost SAR imagery and continuing the path forward to developing reliable passive bistatic SAR systems.

1.1 Problem Statement

1.1.1 Heterogeneous Clutter.

The current body of knowledge regarding SAR primarily regards fine resolution for imaging applications [6], [7], as shown in Fig. 1(a), but this thesis is concerned with coarse resolution cells. As the size of the resolution cell increases, it becomes more likely to contain multiple clutter types. Fig. 1(b) illustrates the composition of a larger background cell with heterogeneous clutter.

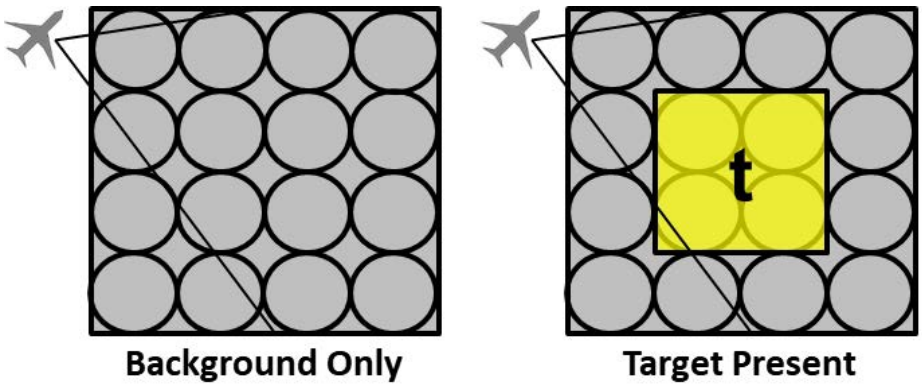

(a) Fine resolution sensor and homogeneous clutter background with many resolution cells (represented by the circles)

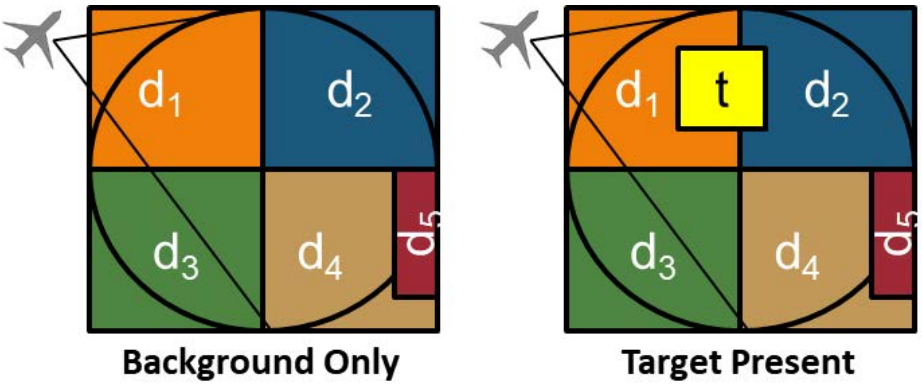

(b) Coarse resolution sensor and heterogeneous clutter background within one resolution cell; each section d_1 through d_5 represents a different clutter type and section t represents a target of interest

Figure 1: Each circle represents the scope of one resolution cell. Fine resolution cells are typically comprised of a homogeneous clutter background or a target of interest which engulfs multiple resolution cells. Coarse resolution cells are more apt to contain heterogeneous clutter than fine resolution cells, and a target of interest may not entirely fill the cell [5] (used with permission of author).

1.1.2 Model Mismatch.

SAR target detection does not abide by the same hypotheses which are typically used in signal detection theory. Basic theory considers the following hypotheses [5]:

$$\begin{aligned} H_0 &: \text{return} = \text{clutter} + \text{noise} \\ H_1 &: \text{return} = \text{clutter} + \text{noise} + \text{target} \end{aligned} \tag{1}$$

This does not reflect the reality of a low-resolution detection scenario. Unlike audio or many radio frequency (RF) detection applications, where signal and unwanted noise or clutter can coexist within the same return, a SAR target occupies physical space and displaces a portion of the clutter. Thus, a more appropriate hypothesis test to perform is:

$$\begin{aligned} H_0 &: \text{return} = \text{clutter} + \text{noise} \\ H_1 &: \text{return} = \text{reduced clutter} + \text{noise} + \text{target} \end{aligned} \tag{2}$$

Any detector that relies upon the hypotheses in Eq. (1) introduces model mismatch, which distorts the receiver operating characteristic (ROC) curve and provides a decision threshold that does not provide the requisite probabilities of detection and false-alarm [5].

1.2 Research Goals and Contributions

This thesis develops a model which compensates for mismatch and determines the detection thresholds appropriately. The primary goal is to simulate a resolution cell containing heterogeneous clutter, then develop a methodology for combining the individual probability distribution function (PDF) of each clutter type into a single

PDF representative of the entire cell. Besides return from the target itself, there will be a shadowing effect due to the receiver getting no return from the patch of clutter behind the target. By leveraging this absence of clutter return, the model estimates which portion of the original clutter has been replaced with a shadow. In conjunction with a land cover map or previously-collected overhead imagery, the replaced clutter profile can refine the target location within the large resolution cell.

1.2.1 Low-cost Imagery.

There are several incentives to pursue low-cost imagery collection; the primary obstacle to pursuing this is the relative inability to detect targets in low-resolution scenarios. This thesis provides a methodology for detecting and locating targets within large resolution cells, which reduces the necessity of using expensive, high-bandwidth radar equipment.

1.2.2 Detection Theory.

The position of a target within a heterogeneous clutter cell influences the statistical properties of the signal return. This thesis demonstrates the procedure for executing a detection hypothesis test when the statistics of the target-present scenario are variable.

1.2.3 SAR Super-Resolution.

A low resolution SAR image gives a poor estimate for the position of a target which is located within. This thesis provides a methodology to reduce the amount of positioning error for a target in a low resolution image.

1.2.4 Passive Bistatic SAR.

While the experiments in this thesis do not incorporate bistatic scenarios involving an emitter of opportunity, the concept of detecting targets in heterogeneous, low-resolution clutter will be an important foundation of that study. Utilizing passive bistatic platforms will allow the radar receiver to collect imagery through hostile territory with a lower risk of intercept.

1.3 Assumptions and Limitations

1.3.1 Clutter Maps.

The following experiments are highly dependent on prior knowledge of the clutter background composition. The return from a specific clutter type can often be expressed as a realization from the distribution of a random variable. For example, the magnitude of a return from a section of the ocean could be shown as a Weibull-distributed random variable with parameters $a = 10125, b = 2.17$ [8]. The mass of water in the sea can be modeled as an array of individual point scatterers whose combined return magnitude from a specified area measurement (e.g. 1 m^2) follows the Weibull distribution. These experimental distributions for general clutter types can be combined with detailed maps which show the geographical boundaries of each clutter type. It is therefore assumed that the resolution cell of interest can be mapped showing the type of clutter that exists throughout the cell, and that the detection and estimation experiments apply to scenarios in which the clutter map is available.

1.3.2 Target Identification.

In a similar fashion, this thesis also assumes that the distribution and size for any target of interest are also known. The parameters used for both target and clutter

distributions are realistic and illustrate the influence of each parameter on the overall model.

1.3.3 SAR Collection.

Ideally, the SAR receiver collects as many pulses as possible in order to build a robust data set for accurate detection and position estimation decisions. However, the following experiments operate under the assumption that the receiver can collect a limited number of pulses. The cross-range resolution of a SAR image is defined by the azimuth support of the receiver, and low cross-range resolution implies that the receiver is collecting over a small support angle, and therefore collects few pulses. It is assumed that the SAR images used to perform the detection test are independent and identically-distributed. Furthermore, it is assumed that there are no complications preventing the SAR data from being properly collected; the focus is instead on the statistical properties of the heterogeneous clutter cell and the techniques used to develop a target detector.

1.4 Thesis Organization

This thesis is organized into five chapters. Chapter II will cover generalized concepts for clutter modeling and target detection, as well as similar previous research. Chapter III outlines the methodology that was undertaken to run the necessary experiments. Chapter IV will showcase and analyze important test results. Chapter V serves as a summary offering relevant conclusions and recommendations for future work.

II. Background, Literature Review, and Related Research

This research relies on background knowledge in a number of fields, including SAR, radar clutter modeling, detection theory, shadow tracking, and image super-resolution. The works referenced in this chapter will lay the groundwork for the research methodology.

2.1 Synthetic Aperture Radar Principles

2.1.1 Low-Resolution Scenarios.

There are two primary reasons why a radar would have to contend with low resolution: the radar is built using inexpensive hardware with a limited bandwidth (a more prevalent concern in a monostatic scenario), or the receiver is utilizing signals of opportunity, many of which are not optimized for high bandwidth (unique to a bistatic radar case).

A SAR grid can be laid out as shown in Fig. 2, with range in the dimension normal to the radar boresight and cross-range in the direction of flight. The receiver is aboard a controllable mobile asset with a side-looking airborne radar (SLAR).

2.1.2 Range Resolution.

The range resolution (R_{res}) of a SAR image is a function of the signal bandwidth. The monostatic equation for radar range resolution is

$$R_{res} = \frac{c}{2B} \tag{3}$$

where B is the signal bandwidth and c is the speed of light [9]. Table 1 shows the bandwidths and corresponding range resolutions of several common communications

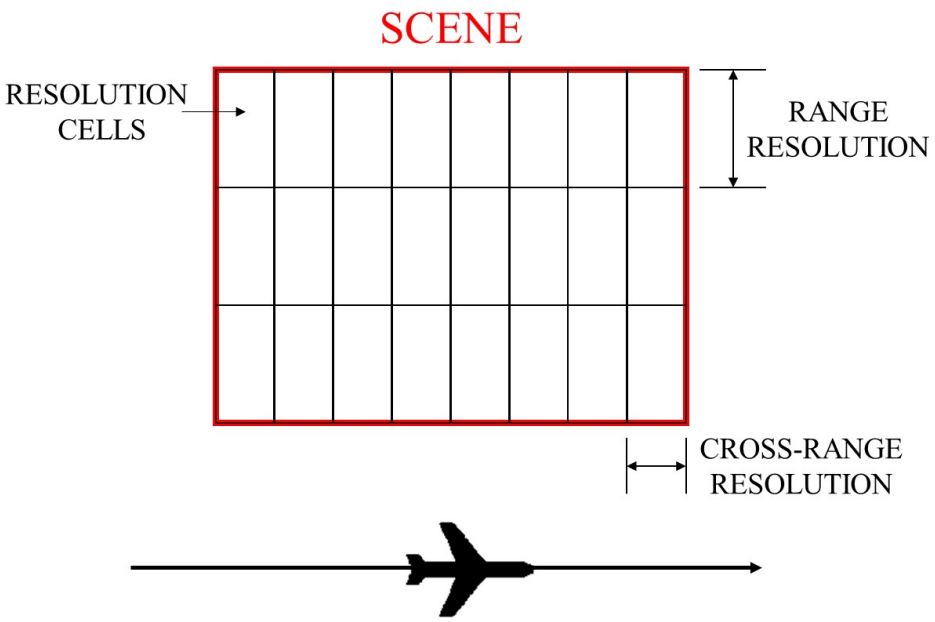

Figure 2: Range and cross-range references relative to the flight path of the receiver

signals that are widely available for use, including Digital Audio Broadcast (DAB), Digital Video Broadcast (DVB), and Long-Term Evolution (LTE) [10].

Table 1: Maximum bandwidth for signals of opportunity

Signal Type	Bandwidth	Range Resolution
DAB	1.537 MHz	97.53 m
DVB	7.608 MHz	19.70 m
LTE	19.815 MHz	7.56 m

2.1.3 Cross-Range Resolution.

Unlike the range resolution, the cross-range resolution (CR_{res}) is independent of the bandwidth and is instead dependent on the parameters of the receiver. The

expression for monostatic cross-range resolution is

$$CR_{res} = \frac{c}{2f_c\theta} \tag{4}$$

where f_c is the carrier frequency and θ is the azimuth support of the system in radians [11]. A suitable carrier frequency for the LTE waveform is 728 MHz [12]. Thus, for a 1° azimuth support, the cross-range resolution is approximately 11.80 meters, and any change in the azimuth support would yield an inversely proportional response to the cross-range resolution.

2.1.4 Un-aliased Scene Extent.

There is a limit to the extent of the SAR image scene that can be processed before aliasing begins to occur. In the range dimension, this is

$$W_R = \frac{c}{2\Delta f} \tag{5}$$

where W_R is the scene extent in the range dimension and Δf is the spacing between frequency bins used in the fast Fourier transform (FFT) for processing the SAR image. In the cross-range dimension, the maximum extent is

$$W_{CR} = \frac{c}{2f_c\delta} \tag{6}$$

where W_{CR} is the scene extent in the cross-range dimension and δ is the angular spacing between consecutive pulses used in the SAR image [13].

2.2 Shadow Detection and Tracking

A classical detection model would be similar to Eq. (1), as found in [14]. This model assumes the same level of clutter in both hypotheses. A new model must be derived to account for scenarios in which some of the original clutter is not reflected toward the receiver because it is obstructed by the target. This consists of the area upon which the target is sitting as well as the ground which is blocked from the radar's line-of-sight due to the height of the target. This section of obstructed clutter is referred to as the shadow.

Shadow tracking is an emerging interest within the SAR field of study because of the utility in detecting and tracking moving objects. The SAR backprojection algorithm cannot resolve the location of a moving target. The shadow region is unique in a SAR image because of its absence of clutter; often, shadows are more discernible than the target creating them [15], [16]. The shadow can still lend information about the target in this thesis despite that it is stationary.

Per [17], multiple look-angles can be leveraged to accurately determine the length of a shadow. Coupled with a known grazing angle, the height of the target can then be determined. The shadow can be useful for bypassing intricate algorithms to estimate the target height.

2.3 Clutter Modeling

The overall SAR image can be broken down as illustrated in Fig. 3. The entirety of the area to be imaged is referred to as the scene. The gridlines denote the range and cross-range bins which form the resolution cells. Fig. 3(b) shows the clutter regions that exist within the heterogeneous resolution cell.

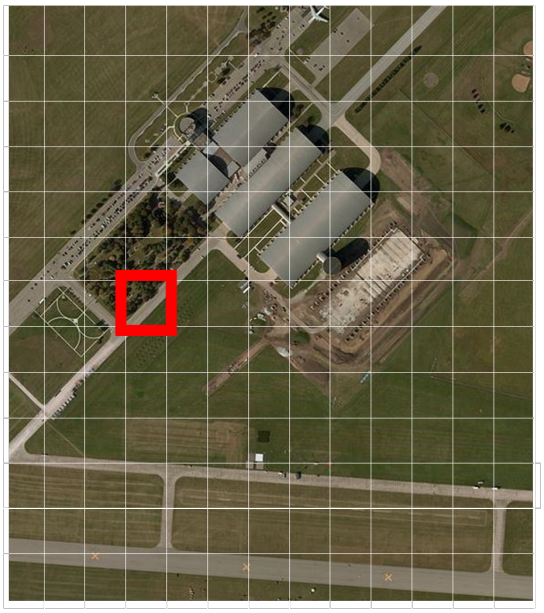

(a) The entire area to be imaged is referred to as the scene. A resolution cell is a portion of the scene which occupies a range bin (defined by the range resolution) and a cross-range bin (defined by the cross-range resolution). A zoomed-in inset of the highlighted resolution cell is shown in Fig. 3(b).

(b) This resolution cell contains three clutter types: foliage/trees (patch 1), concrete (patch 2), and grass (patch 3). This thesis concerns scenes with resolution cells that contain multiple clutter patches. The overall distribution for the radar signal return from this cell is a convolution of the three individual clutter patch distributions relative to their areas.

Figure 3: Example scene and resolution cell grid overlaid on publicly-available satellite imagery of the National Museum of the United States Air Force, WPAFB, OH (from bing.com/maps).

2.3.1 Representation as a Complex Random Variable.

The clutter return from each resolution cell will have a magnitude component and a phase component. Clutter is typically modeled as a spherically-invariate random variable (SIRV), which means that the phase is uniformly distributed [18], [19]. The phase represents the return delay as a fraction of the wavelength. Assuming that the resolution cell is significantly larger than the wavelength, there should be no phase that is more likely than any other since the phase represents a coherent sum of many individual point-scatterers which lie throughout the cell.

The magnitude of the return for a particular clutter type can be parameterized as

a coefficient which represents the strength of the return from a 1 m^2 area of clutter. Therefore, a larger area of clutter is expected to reflect a signal of higher magnitude.

The phase of the return lends no useful information since its distribution is uniform; therefore, the signal return can be represented as a single real-valued magnitude which follows the PDF for some specific random variable. Because this research involves a heterogeneous clutter cell, its distribution function will be a combined PDF of the clutter types and targets which are within the cell. The combined PDF represents a convolution of the individual clutter PDFs, which are scaled by the area of each individual clutter patch; the convolution is performed to obtain a distribution function for the probability of the sum of the scatterers, which represents the total return.

2.3.2 Common Distribution Functions.

Studies such as [20], [21], and [22] suggest the Rayleigh distribution as a basic yet useful framework for modeling clutter. This is because the Rayleigh distribution is derived from Gaussian components, a common distribution of study due to the central limit theorem (CLT) [23]. The Weibull distribution is more versatile because it includes an additional 'shape' parameter b in addition to its 'scale' parameter a, for which the Rayleigh is a special case ($b = 2$) [24]. Thus, the Weibull distribution can characterize Rayleigh-distributed clutter as well as other clutter types with varying shape parameters.

Perhaps the most useful aspect of the Rayleigh distribution is that its real and imaginary components are Gaussians and can be summed together (as would occur when the scattering returns from multiple clutter types are summed in a single radar resolution cell) to form another Gaussian. The summed real and imaginary Gaussians combine to create a random variable with Rayleigh-distributed magnitude and a

uniform phase, assuming that the original variables are independent of one another. The PDF can then be expressed in terms of the parameters defined by the individual clutter types.

For other b values of the Weibull distribution, there is not a definitive method for summing the independent random variables into a closed form [25]. As a result, it is necessary to estimate the sum of multiple complex Weibull-distributed independent random variables as some other distribution.

Fig. 4(a) and Fig. 4(b), respectively, show isometric and overhead views of the 2-dimensional PDF for a Weibull-distributed random variable with parameters $a = 5,\ b = 5$. The expected value of the random variable is indeed zero; this is due to an equal probability of positive and negative values. The magnitude, however, is highly unlikely to be near zero.

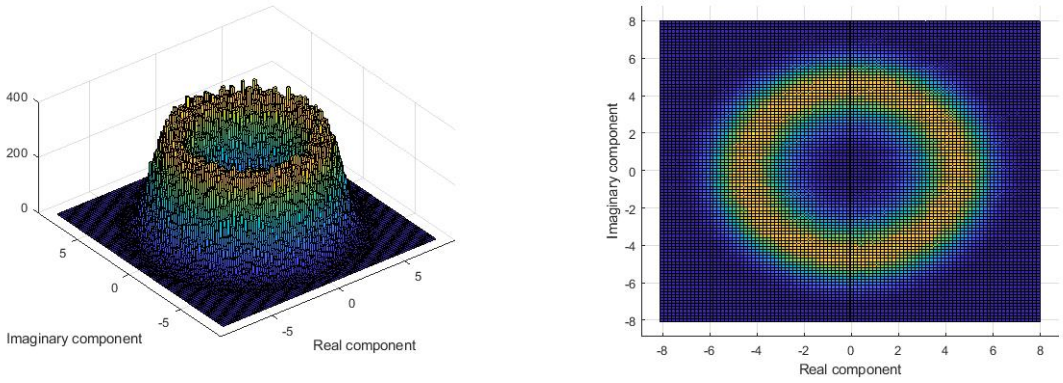

(a) Isometric view

(b) Overhead heat map

Figure 4: Histogram of a complex random variable which is Weibull-distributed in magnitude with $a = 5, b = 5$, and uniformly distributed in phase modeling a 2-D PDF.

In order to obtain a joint PDF for the various types of clutter which are in the target cell, it is necessary to convolve the individual PDFs together.

The PDF for a Weibull distribution is

$$f_x(x) = \begin{cases} \frac{b}{a}\left(\frac{x}{a}\right)^{b-1} e^{-(x/a)^b} & x \geq 0 \\ 0 & x < 0 \end{cases} \tag{7}$$

where x is a realization of the Weibull distribution, a is the scale parameter, and b is the shape parameter.

If there are two distinct clutter patches within a resolution cell which are independent from each other, their convolution can be expressed as

$$f_x(x) = \int_{-\infty}^{\infty} \left(\frac{b_1}{a_1}\left(\frac{s}{a_1}\right)^{b_1-1} e^{-(s/a_1)^{b_1}}\right)\left(\frac{b_2}{a_2}\left(\frac{x-s}{a_2}\right)^{b_2-1} e^{-((x-s)/a_2)^{b_2}}\right) ds \tag{8}$$

where the subscript after each a and b term represents the coefficient for the corresponding clutter patch.

If there are more than 2 clutter patches within the resolution cell, multiple iterations of this convolution process will be performed. The $\bigstar$ symbol is used to notate repetitive convolution. For example,

$$\bigstar_{k=1}^{4} f_{x_k} = ((f_{x_1} * f_{x_2}) * f_{x_3}) * f_{x_4} \tag{9}$$

where $*$ indicates the convolution of two functions.

The PDFs must be scaled to account for the area occupied by each clutter patch (A_k). One property of the Weibull distribution is that multiplying the scale factor a by A_k yields the same PDF as would be derived by stretching and scaling the original

PDF by A_k. This derivation can be shown as

$$f_x(x; b, a) = \frac{b}{a}\left(\frac{x}{a}\right)^{b-1} e^{-(x/a)^b}$$
$$f_x(x; b, A_k a) = \frac{b}{A_k a}\left(\frac{x}{A_k a}\right)^{b-1} e^{-(x/(A_k a))^b} \tag{10}$$

If $x' = \frac{x}{A_k}$, then the expression reduces to

$$\begin{aligned} f_x(x; b, A_k a) &= \frac{1}{A_k}\frac{b}{a}\left(\frac{x'}{a}\right)^{b-1} e^{-(x'/a)^b} \\ &= \frac{1}{A_k} f_{x'}(x'; b, a) \end{aligned} \tag{11}$$

The expression for the PDF of the scene without targets would then be

$$f_x(x) = \bigstar_{k=1}^{K} f_{x_k}(x_k; b_k, A_k a_k) \tag{12}$$

where K is the number of clutter patches within a resolution cell.

2.4 Target Modeling Techniques

The geometry of the target greatly influences its model. The target radar cross-section (RCS), combined with the angle of reflection with respect to the receiver, dictate the distribution of the scattering returns [27]. Because it is impossible to consider all target RCS signatures in this thesis, the target is modeled as an object which has relatively similar scattering profiles at all look-angles.

Clutter can be modeled as a scatterer with uniform height, and the clutter return can be assumed to come from a two-dimensional area of clutter, rather than a three-dimensional volume. A target, contrarily, will typically stand above the clutter, such as a vehicle on a concrete runway, or a weapon in a field of grass. Since a SAR receiver

is an airborne platform, it is physically closer to the top of the target than the bottom of a target and clutter. If the height of the target is neglected (set equal to 0), the one-way differential from the target to the scene center in a monostatic scenario is

$$t = \frac{\sqrt{\text{range}^2 + \text{cross-range}^2}}{c} \tag{13}$$

[28]. Accounting for the differential in height, the one-way differential from the target to the scene center in this case is

$$t = \frac{\sqrt{\text{range}^2 + \text{cross-range}^2 + h^2}}{c} \tag{14}$$

where h is the height of the target [28]. The vertical dimension of the target must be conveyed onto the 2-D surface based upon the equivalent one-way delay. In some cases, the return from the top of the target may appear in a neighboring resolution cell. The area of clutter which reflects signal back to the radar corresponds to the area on the ground occupied by the clutter. The area of the target which reflects signal to the radar is the apparent surface area of the target from the perspective of the radar. The differential between the physical area of the target and the effective area of the target can be expressed as A_{ov}. This is the overlay area for which the target reflection overlays the clutter reflection at an equivalent delay.

Once a target is introduced, Eq. (12) is modified to include the return from the target as

$$f_x(x) = \left[\bigstar_{k=1}^{K} f_{x_k}(x_k; b_k, A_k a_k) \right] * f_{x_t}(x_t; b_t, (A_t + A_{ov}) a_t) \tag{15}$$

where A_t is the area of the target on the ground.

This notation cannot be expressed in closed form [26], so the results will be obtained computationally through simulation and use of MATLAB. The matrix math

used to simulate the signal return is discussed in Chapter 3. The work in Chapter 3 also accounts for area of clutter which is obstructed by the target and its shadow.

2.5 Target Detection and Estimation Schemes

An ideal detection scheme would be capable of positively identifying every target without any false alarms. Due to the random nature of clutter and target returns, this is an impossible task, so the question arises as to how to most efficiently identify targets. Several methodologies for detection will be explored.

2.5.1 LRT Detector.

The likelihood ratio test (LRT) can be used to determine whether it is more likely that a target is present or absent. The likelihood ratio is calculated as

$$\Lambda(S) = \frac{p(S|H_1)}{p(S|H_0)} \tag{16}$$

where S is the test statistic and Λ is the likelihood ratio. [29], [30]. The likelihood test calculates the ratio of the PDFs under the conditions of H_0 and H_1 given the test statistic S. The likelihood threshold λ is a predetermined value which is calculated from the relative cost of missed detections and false alarms as well as the prior probabilities of H_0 and H_1. If the ratio exceeds (or, in some cases, is less than) λ, a detection is declared.

2.5.2 Multiple Hypothesis Detection Scheme.

The likelihood ratio derivation described above is a binary detection scheme; the target is declared to be either present or absent. A multiple hypothesis detection scheme can be used to predict the position of a target in the scenario where it has been previously determined that a target is present within the resolution cell. Rather

than expressing the target coordinates as continuous values, discrete positions can be assigned to define potential target locations. In Fig. 3(b), 3 positions to choose from include: within clutter patch 1, within clutter patch 2, or within clutter patch 3. The detection is performed based upon the cost matrix of incorrectly guessing the position as well as the prior probability of the target appearing at each location. The multiple hypothesis detector minimizes risk ($\mathcal{R}$), which is expressed as

$$\mathcal{R} = \sum_{i=0}^{Y-1} \sum_{j=0}^{Y-1} C_{ij} P(\mathcal{H}_i|\mathcal{H}_j) P(\mathcal{H}_j) \tag{17}$$

where C_{ij} is the cost of choosing H_i when H_j is the true hypothesis and Y is the number of target positions considered [30].

This is a simple breakdown of the multiple hypothesis detection; more target locations could be considered, such as a position where the target is straddling clutter patches 1 and 2. Adding more positions refines the estimated location of the target but adds increased computational complexity as the cost matrix expands with each additional position that is considered.

III. Methodology

This thesis can be separated into two focuses:

- a detection problem concerned with the presence or absence of a target within a resolution cell which has various clutter sections of known parameters
- an estimation problem for which the output is an estimate of the amount of each clutter type present in the resolution cell, from which the relative position of the target can be extrapolated

The detection experiment objectives are to develop ROC curves for heterogeneous clutter models which correct the mismatch present in traditional detection models and to determine the effects of changing key parameters within the resolution cell.

The estimation focus allows for a more accurate target position estimate in an otherwise low-resolution cell. This experiment is more computationally intensive than the binary detection because numerous thresholds must be determined to differentiate between target locations.

3.1 Simulation Setup

Many of the parameters used to set up the experiment simulation are the same for both approaches.

3.1.1 SAR Receiver Parameters.

In a SAR image, multiple pulses must be collected in order to form the synthetic aperture. In a detection problem with random variables, multiple repetitions of the data collection are necessary to better differentiate between H_0 and H_1. One way to achieve this would be to fly past the scene many times and create a SAR image each

time. This is not efficient. A more tangible approach is to split the overall aperture into sub-apertures. Each sub-aperture generates data for each resolution cell in the scene, and the data from each sub-aperture is combined to make a detection decision. It is assumed that the number of pulses used to build the sub-aperture SAR image does not impact the distribution of each clutter or target type.

3.1.1.1 Sub-aperture Requirements and Considerations.

Fig. 5 shows two potential methods for separating the collected pulses into sub-apertures. Fig. 5(a) shows a scenario where the pulses are consecutively grouped into sub-apertures. A benefit to this arrangement is that it reduces the amount of correlation between sub-apertures. In analyzing the signal return, independence and identical distribution are key assumptions.

Fig. 5(b) uses an interleaving method to assign sub-apertures. Because the collected pulses from sub-aperture 1 and sub-aperture 2 are physically so close to each other, there is a greater likelihood of correlation between the returns from those sub-apertures. The primary advantage of interleaving the sub-apertures is an immense increase in azimuth support. In Fig. 5(a), each circle along the flight path of the aircraft represents a collected pulse, and each color represents a new sub-aperture. The support for each of the 4 sub-apertures, denoted by θ_s, is approximately 1/4 of the overall azimuth support. In Fig. 5(b), the spacing between the 1st and last pulses from each sub-aperture spans nearly the entire aperture. This greatly improves the cross-range resolution. In order to sharply increase the number of sub-apertures available for analysis, thereby increasing detection accuracy, the interleaved method becomes necessary.

There is a limit to the width of the overall aperture; the clutter and target may have different RCS signatures at different viewing angles. It is necessary to assure

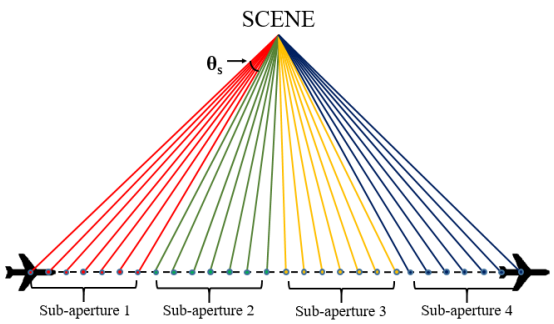

(a) Sub-apertures arranged consecutively within a synthetic aperture - 28 pulses, 4 sub-apertures

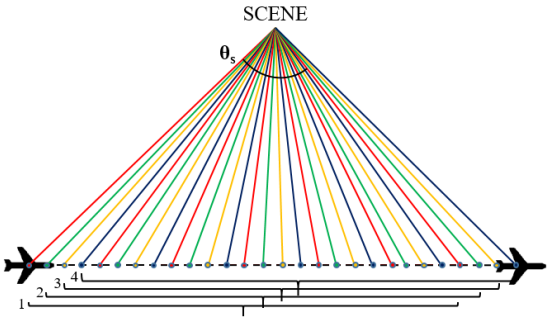

(b) Sub-apertures interleaved amongst one another to increase azimuth support angle - pulses of the same color belong to the same sub-aperture

Figure 5: The collection of pulses can be organized such that the sub-apertures are interleaved with one another. This increases the angle of support for each sub-aperture without reducing the number of pulses per sub-aperture. With the consecutive method, there may be differences in scattering statistics as the look-angle changes between sub-apertures.

independence by spacing the pulses adequately but also to maintain an identical distribution between sub-aperture returns. As long as the overall aperture is less than 10°, the assumption will be kept that this difference will not vastly impact the clutter model.

3.1.1.2 Sub-aperture Assignment.

The number of pulses collected per sub-aperture determines the extent of the unaliased SAR image scene. As discussed in Chapter 2, the spacing between pulses for each sub-aperture determines the extent of the scene in cross-range, which is

$$W_{CR} = \frac{c}{2f_c\delta} \tag{18}$$

Since the cross-range of a resolution cell is $\frac{c}{2f_c\theta_s}$, the number of resolution cells within the scene extent in the cross-range dimension can be expressed as $\frac{\theta_s}{\delta}$. If there are only 2 pulses, then $\theta_s = \delta$, so there is only one cell in the cross-range dimension of

the scene. Because this thesis is focused on the scattering characteristics of a single resolution cell, only two pulses are needed to create a sub-aperture. Using the interleaving method with 2 pulses per sub-aperture produces a sub-aperture arrangement as shown in Fig. 6.

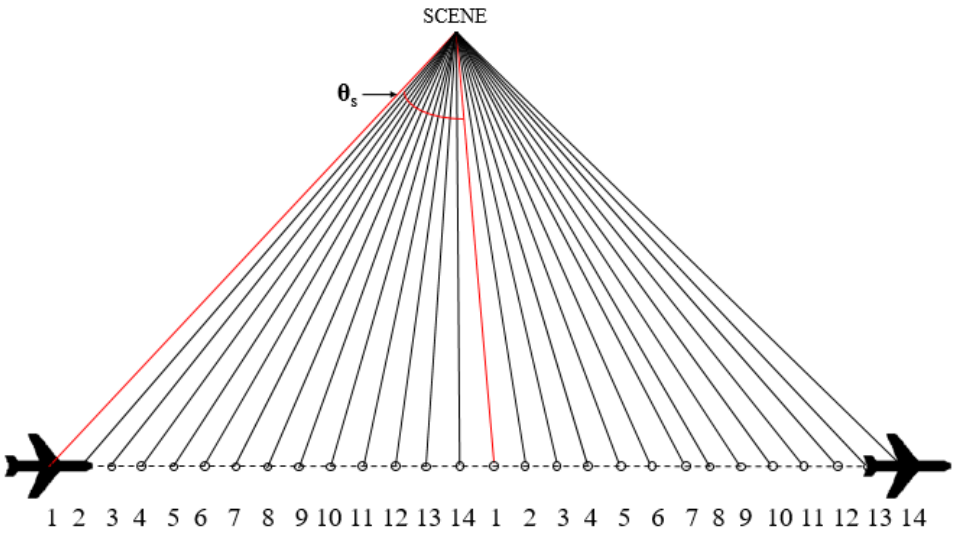

Figure 6: Each sub-aperture consists of two pulses in the following experiments. Placing the sub-apertures too close together carries a risk of correlation, but the assumption will be made that the sub-apertures are independent of one another.

3.1.1.3 Resolution Cell.

In this thesis, an LTE waveform will be used. This is one potential signal of opportunity, and a limited-bandwidth, low-cost monostatic transmitter/receiver could have a similar bandwidth. The bandwidth and carrier frequency of the signal determine range resolution and cross-range resolution for the radar, as discussed in Section 2.1. The effective bandwidth of an LTE signal is 19.815 MHz, giving a range resolution of 7.56 m. Among common communication signals, this yields the finest range resolution; the range resolutions for DAB and DVB signals can be calculated using the information from Table 1.

The cross-range resolution is dependent upon the extent of the sub-aperture azimuth support. This is customizable based upon the considerations listed in the previous subsections. If there are m pulses which are collected across the entire aperture and N sub-apertures, this leaves $\lfloor \frac{m}{N} \rfloor$ pulses per sub-aperture. It also means that the number of pulses separating the first and last pulses from each sub-aperture is $m - N$ in the interleaved case. Therefore, the azimuth support for each sub-aperture is $\theta_s = \theta(1 - \frac{N}{m})$. As N decreases, the azimuth support angle for each sub-aperture increases, improving the cross-range resolution, but using fewer sub-apertures may deter detection performance. For the 2-pulse interleaved sub-apertures, θ_s is approximately 1/2 of θ.

3.1.1.4 Data Collection.

The aperture collection geometry will dictate the amount of data which is available for analysis. The total number of pulses collected is a function of the total radar azimuth support in radians (θ), the velocity of the collection platform (v), the radar range (R) and the pulse repetition frequency (PRF) of the radar. The total number of pulses can be expressed as

$$m = \frac{\theta R f_{PRF}}{v} \tag{19}$$

where f_{PRF} is the radar PRF.

3.1.2 Clutter Modeling.

The distributions used to model clutter are representative of the expected phase and magnitude for an entire SAR sub-aperture image. The model used is for the expected distribution for the patch of clutter after the image is formed, not for individual pulse returns.

Clutter is modeled in MATLAB as a SIRV which is Rayleigh-distributed in magnitude, as a special case of the Weibull distribution. The values used to represent the distribution of the clutter magnitude are based upon a clutter area of 1 m^2. While, practically, a single magnitude and phase are returned to the receiver from each resolution cell, the MATLAB simulation will model the return as individual point-scatterers (one for each clutter type, target, and shadow) which are then scaled by area and summed into one complex value.

In a noise-free environment without any targets present, the heterogeneous resolution cell consists solely of its multiple clutter types. Each clutter patch is represented by its scattering distribution and area. The returned signal is the sum of the return from each individual clutter patch and can be represented as

$$S_r = \sum_{k=1}^{K} A_k W(a_k, b_k) \tag{20}$$

where S_r is the received radar return and $W(a_k, b_k)$ is a realization from a Weibull-distributed random variable with shape and scale parameters specific to the k^{th} clutter patch, multiplied by a realization from a random uniform phase. The return can be expressed as such because the parameters which define the distribution for each clutter type are based on a coefficient relative to a 1 m^2 section of clutter. Each 1 m^2 section is assumed to reflect the same magnitude and phase back to the radar, so the total return from the clutter patch has a linear relationship with its area.

S_r can also be expressed in matrix notation by separating the summed terms into

an area vector $\mathbf{A}$ and a realization vector $\mathbf{W}$, as

$$S_r = \begin{bmatrix} A_1 & A_2 & ... & A_K \end{bmatrix} \begin{bmatrix} W(a_1, b_1) \\ W(a_2, b_2) \\ ... \\ W(a_K, b_K) \end{bmatrix} \tag{21}$$

Once a target is introduced to the cell:

- The target occupies some area A_t and displaces some of the area of the clutter.
- There exists a shadow area on the ground A_s for which the receiver does not receive any signal reflection since its line-of-sight is obstructed by a target of non-zero height.
- The area of each clutter patch is reduced by some value ϵ_k.

The collection of ϵ_k values can be combined into a single vector $\boldsymbol{\epsilon} = [\epsilon_1, ..., \epsilon_K]$. The ϵ_k values are subtracted from their respective A_k values in the area vector. Additional entries in the area vector are created for the target and the shadow. In the realization vector, a value is added for a Weibull-distributed target magnitude, which is also modeled as a SIRV. An entry of zero is added into $\mathbf{W}$ for the shadow since there is zero return from the shadow area. In a target-present scenario, S_r can be expressed as

$$S_r = \begin{bmatrix} A_1 - \epsilon_1 & A_2 - \epsilon_2 & ... & A_K - \epsilon_K & A_t & A_s \end{bmatrix} \begin{bmatrix} W(a_1, b_1) \\ W(a_2, b_2) \\ ... \\ W(a_K, b_K) \\ W(a_t, b_t) \\ 0 \end{bmatrix} \tag{22}$$

Removing A_s from $\mathbf{A}$ and the corresponding 0 from $\mathbf{W}$ does not have any effect on the outcome of S_r, but it allows the sum of $\mathbf{A}$ to remain constant since

$$A_t + A_s = \sum_{k=1}^{K} \epsilon_k. \tag{23}$$

This varies from the body of previous work discussed in Chapter 2 in that Eq. (15) does not account for the area of each clutter patch which is displaced by the target and its shadow.

3.1.3 Shadow Simulation.

If the target of interest is elevated above the rest of the scene, there will be some area on the ground for which no return is scattered toward the receiver because the target blocks that line of sight. In a bistatic scenario, there is another shadow beyond the target from the field of view of the transmitter. The amount of shadow which a single target creates is heavily dependent upon the bistatic geometry. Fig. 7 shows the shadows that result from the transmitter and the receiver. To simplify, this experiment considers a psuedo-monostatic case in the development of the shadow.

In the psuedo-monostatic case, the vertical surface of the target also contributes extra visible surface area from the receiver perspective. The top of the target is closer in range to the airborne receiver than the ground clutter. When the height of the target is conveyed onto a 2-dimensional space, the return from the top of the target and the clutter in front of the target are received at an equivalent delay. Fig. 8 illustrates a side and top view of how the returns from each section are processed when converted from three dimensions to a typical 2-D SAR image.

Fig. 9 shows a square resolution cell with a different clutter type in each quadrant, a red target, and a dark blue sector behind the target representing the shadow - there is zero return from those scatterers on the ground. In any MATLAB figure showing

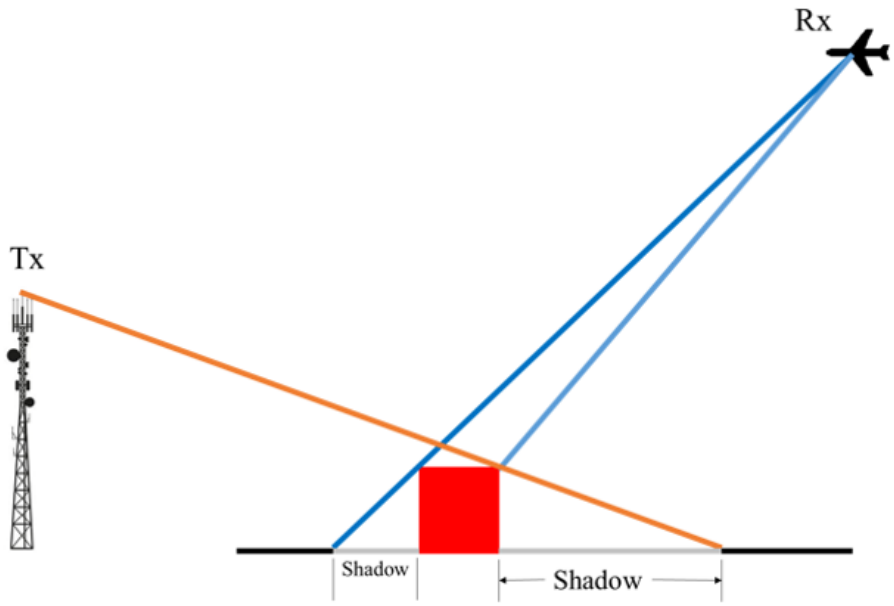

Figure 7: Because the target sits above the ground, there are point-scatterers nearby whose path from the transmitter to the receiver is obstructed by the target. This diagram illustrates a bistatic angle of 180°.

clutter and targets, the magnitude of the return from any of the sub-pixels is indicated by a blue-to-red spectrum, where darker blues indicate the lowest values of return and dark red sub-pixels have high return.

The shadow area is

$$A_s = \frac{hR}{Z}\ell_{CR}(\phi) \tag{24}$$

where R is the one-way radar range, Z is the altitude of the radar, and $\ell_{CR}(\phi)$ is the length of the target in the cross-range dimension, as a function of look-angle ϕ. The simulated area of the target overlay (A_{ov}) is the differential between the physical area of the target on the ground and the perceived area from the receiver due to the height of the target; it is very dependent upon the geometry of the target. A simple mixing model is used to add the return from the target to the existing clutter at an equivalent delay.

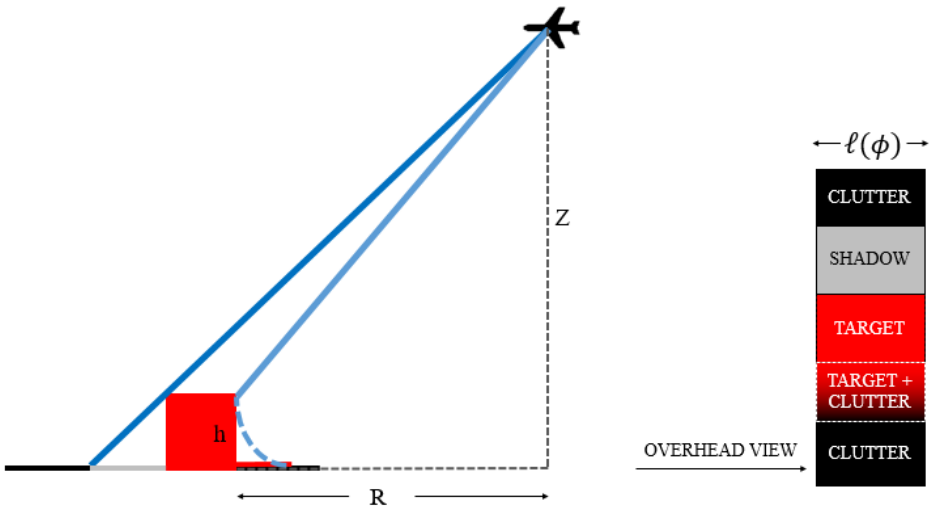

Figure 8: Illustration of how some clutter lies in the shadow of the target, while other clutter is at the same range as the target.

3.1.4 Noise Figure.

There is also white noise to consider in the model, which can be assumed as additive white Gaussian noise (AWGN). The noise is zero-mean; its variance is determined by the signal-to-noise ratio (SNR) of the imaging environment. The noise, along with the target overlay area determined in the previous subsection, is added onto the overall return from Eq. (22) as

$$S_r = \begin{bmatrix} A_1 - \epsilon_1 & \dots & A_K - \epsilon_K & A_t + A_{ov} & A_s \end{bmatrix} \begin{bmatrix} W(a_1, b_1) \\ W(a_2, b_2) \\ \dots \\ W(a_K, b_K) \\ W(a_t, b_t) \\ 0 \end{bmatrix} + V \tag{25}$$

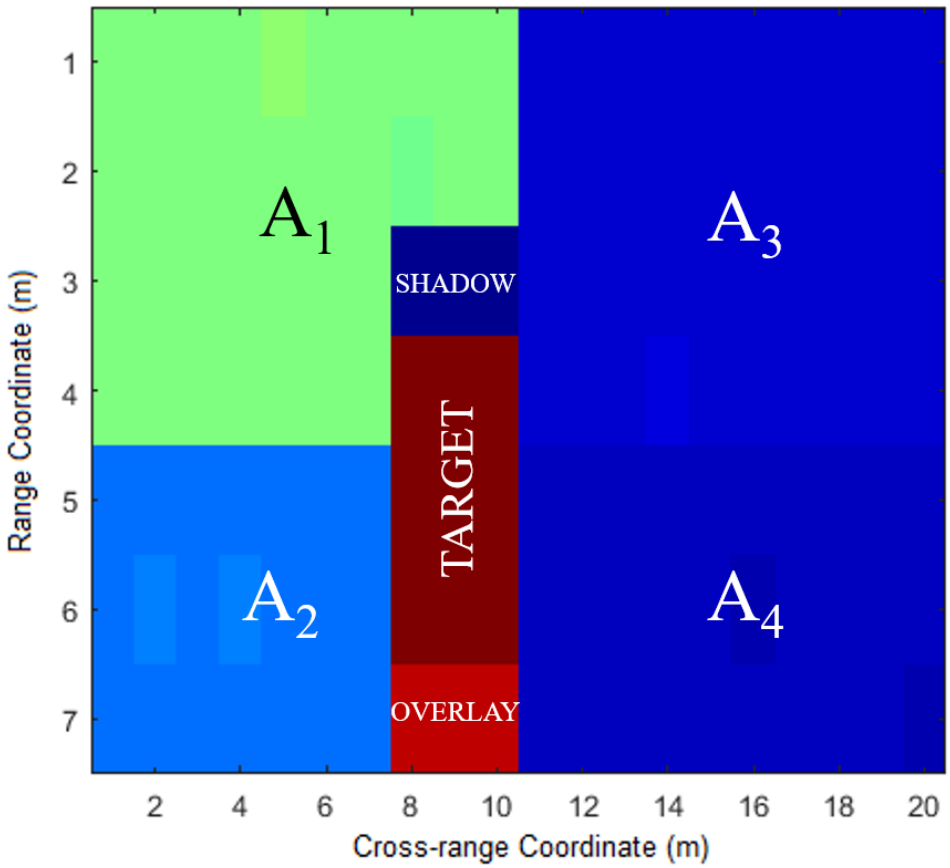

Figure 9: Map of simulated clutter and target - the dark section above the darkest red area represents the target's shadow; the red shade below the dark red indicates that the specific range represented by that scatterer is occupied by both clutter and the target. The receiver is along the bottom of the figure.

where V is the representation for the noise with the complex normal distribution $V \sim CN\left(0, \sum_{k=1}^{K} A_k \sigma_n^2 \underline{\underline{I}}\right)$. Expressing the noise in this way allows for the magnitude of the noise power per m^2 to be a Rayleigh distribution with coefficient parameter σ_n. The noise power is expressed in terms of the power density so as to be more easily comparable with the target and clutter magnitudes, which are also functions of their areas. This allows for a simple computation of the SNR.

3.1.5 MATLAB Representation.

All of the computation and simulation of the radar environment is performed in MATLAB. A matrix is used to depict the scattering characteristics of the resolution cell; each entry represents a 1 m $\times$ 1 m sub-pixel and is assigned a value based upon whether that area is occupied by clutter, target, or a shadow. The return from each clutter patch is modeled as a product of a random realization from a distribution with parameters based on its model and its area, as described in Eq. (21). This is achieved by assigning the same value, randomly drawn from a specified distribution, to each sub-pixel within the clutter patch.

If a target is introduced, the target replaces the clutter values previously assigned to the applicable sub-pixels. The target height, platform altitude, one-way radar range, and receiver look-angle determine the extent of the shadow. The value for the sub-pixels in the shadow region is zero.

Finally, AWGN is added to each sub-pixel. In order to represent the noise similarly to the clutter return, the σ_n^2 value is a noise power density. A random realization from a complex Gaussian with covariance $\sigma_n^2 \underline{\underline{I}}$ is added to each 1 m^2 sub-pixel. The noise realization for each sub-pixel is independently drawn from the complex Gaussian distribution.

The sum of all entries in the matrix representing the resolution cell is the total return received, and is the only information which would be available to a real-world SAR receiver.

3.2 Target Detection

3.2.1 Clutter and Target Models.

The mechanics behind combining multiple complex non-Gaussian distributions to represent a scene are elaborate, so it is useful to assess less intricate models at a more mathematically robust level. The Rayleigh variant of the Weibull distribution will be used to model clutter and targets. This makes it possible to concisely develop a strong mathematical model. The term 'Rayleigh clutter' will refer to a distribution of clutter which is a SIRV with a Rayleigh distribution in magnitude, a special case of the Weibull distribution where $b = 2$.

The return from a patch of clutter or a target consists of a magnitude and a phase component. The phase represents the fractional wavelength delay in the round-trip path from the transmitter to the receiver. Because the resolution cell is very large and dense with reflective surfaces, it is assumed that one particular wavelength delay is not more likely than any other. Thus, the phase is modeled as a uniform random variable and the clutter distribution is regarded to be a SIRV.

The magnitude of the Rayleigh clutter is defined by the Weibull scale parameter a. It will remain unitless as an area-based coefficient throughout this thesis since the specific unit of signal return is irrelevant. Because the clutter is assumed to be spherically invariant, the real and imaginary components of the return are independent and can be broken down into

$$S_r = I + jQ \tag{26}$$

where I is the real-valued (in-phase) component of S_r and is normally distributed $\sim N(0, \sigma_0^2)$, Q is the imaginary (quadrature) component of S_r and is also normally distributed $\sim N(0, \sigma_0^2)$, and σ_0^2 is the overall variance of each of the real and imaginary

components of the heterogeneous clutter with no target present.

In this SAR collection, multiple sub-aperture images are used as data points. For each image, the returns from individual clutter patches are not measurable and are not distinguishable; only the composite return is measured. A large sample of sub-aperture images is necessary to develop a sufficient statistic for detection purposes.

3.2.2 Hypotheses.

The I and Q components of the return from each clutter patch or target are independent, identically-distributed (i.i.d.) Gaussian random variables because the clutter and target are modeled as SIRVs. It is assumed that the returns from the clutter patches and Rayleigh-distributed target are also independent. Since the I component of the radar return is a sum of independent zero-mean Gaussians, the I portion itself is also a zero-mean Gaussian. The Q component will, likewise, follow the same distribution. Because the composite I and Q portions are independent, identically-distributed Gaussians, $S_r = I + jQ$ is Rayleigh-distributed in magnitude.

The variances of the I and Q components of the return (which are equal given a SIRV Rayleigh distribution) for the no-target case (H_0) and the target-present case (H_1) will be the determining factors in the detection methodology. Let the I-component variance for a cell with no target present be σ_0^2 and the I-component variance for a cell with a target be σ_1^2. Then, the hypotheses are

$$\begin{aligned} H_0 &: |S_r| \sim \text{Rayleigh}(\sigma_0) \\ H_1 &: |S_r| \sim \text{Rayleigh}(\sigma_1) \end{aligned} \tag{27}$$

3.2.3 Likelihood Function.

The likelihood function (Λ) determines the threshold for the detector. The purpose of the likelihood function is to determine which distribution a set of data points from a large number of sub-aperture returns is more likely to have been drawn from. Its calculation is dependent upon independence and identical distribution between signal return pulses. It can be expressed as

$$\begin{aligned}\Lambda(|S_r|) &= \frac{p(|S_r|;H_1)}{p(|S_r|;H_0)} \\ &= \prod_{n=1}^{N} \frac{\frac{|S_{rn}|}{\sigma_1^2}e^{-|S_{rn}|^2/2\sigma_1^2}}{\frac{|S_{rn}|}{\sigma_0^2}e^{-|S_{rn}|^2/2\sigma_0^2}} \\ &= \prod_{n=1}^{N} \frac{\sigma_0^2 e^{-|S_{rn}|^2/2\sigma_1^2}}{\sigma_1^2 e^{-|S_{rn}|^2/2\sigma_0^2}}\end{aligned} \tag{28}$$

where N is the number of SAR sub-apertures and n is the index for each sub-aperture. The likelihood ratio is compared to a likelihood threshold λ to decide between H_0 and H_1. In order to simplify, the inequality can be expressed in terms of a sufficient statistic of S_r compared to a detection threshold γ as

$$\begin{aligned}\prod_{n=1}^{N} \frac{\sigma_0^2 e^{-|S_{rn}|^2/2\sigma_1^2}}{\sigma_1^2 e^{-|S_{rn}|^2/2\sigma_0^2}} &\underset{H_0}{\overset{H_1}{\gtrless}} \lambda \\ 2N\ln\left(\frac{\sigma_0}{\sigma_1}\right) + \left(\frac{1}{2\sigma_0^2} - \frac{1}{2\sigma_1^2}\right)\sum_{n=1}^{N}|S_{rn}|^2 &\underset{H_0}{\overset{H_1}{\gtrless}} \ln(\lambda) \\ \left(\frac{1}{2\sigma_0^2} - \frac{1}{2\sigma_1^2}\right)\sum_{n=1}^{N}|S_{rn}|^2 &\underset{H_0}{\overset{H_1}{\gtrless}} \ln(\lambda) + 2N\ln\left(\frac{\sigma_1}{\sigma_0}\right) \\ \sum_{n=1}^{N}|S_{rn}|^2 &\gtrless \frac{\ln(\lambda) + 2N\ln\left(\frac{\sigma_1^2}{\sigma_0^2}\right)}{\left(\frac{1}{2\sigma_0^2} - \frac{1}{2\sigma_1^2}\right)} \equiv \gamma\end{aligned} \tag{29}$$

In the last line of Eq. (29), the hypotheses are removed from the double inequality symbol; if $\sigma_0^2 > \sigma_1^2$, then the inequality is reversed and the decision of H_1 is made

if the sum of squares is less than the threshold, rather than greater. $\lambda = 1$ if the cost of a missed target and a false alarm are the same and the prior probability of a target being present is $\frac{1}{2}$ or is unknown. Substituting these considerations into the likelihood inequality gives:

$$\begin{cases} \sum_{n=1}^{N} |S_{rn}|^2 \underset{H_0}{\overset{H_1}{\gtrless}} \frac{N \ln\left(\frac{\sigma_1^2}{\sigma_0^2}\right)}{\left(\frac{1}{\sigma_0^2} - \frac{1}{\sigma_1^2}\right)} & \sigma_1^2 > \sigma_0^2 \\ \sum_{n=1}^{N} |S_{rn}|^2 \underset{H_1}{\overset{H_0}{\gtrless}} \frac{N \ln\left(\frac{\sigma_1^2}{\sigma_0^2}\right)}{\left(\frac{1}{\sigma_0^2} - \frac{1}{\sigma_1^2}\right)} & \sigma_0^2 > \sigma_1^2 \end{cases} \tag{30}$$

The sum of squares for each realization of $|S_r|$ is the sufficient statistic. Because $|S_r| = |I + jQ| = |I - jQ|$, where I and Q are independent Gaussians identically distributed as $N(0, \sigma_0^2)$ or $N(0, \sigma_1^2)$,

$$\begin{aligned} \sum |S_{rn}|^2 &= \sum (|I_n + jQ_n|)(|I_n - jQ_n|) \\ &= \sum |I_n^2 + jI_nQ_n - jI_nQ_n + Q_n^2| \\ &= \sum |I_n^2 + Q_n^2| \\ &= \sum I_n^2 + \sum Q_n^2 \end{aligned} \tag{31}$$

This is a sum of squares of independent Gaussian random variables, which forms a χ^2 distribution. Thus, the sufficient statistic $\sum_{n=1}^{N} |S_{rn}|^2$ is a χ^2-distributed random variable with $2N$ degrees of freedom, scaled by the variance of the Gaussian components (σ_0^2 for H_0 and σ_1^2 for H_1). Therefore, the hypothesis test for the sufficient statistic is

$$\begin{aligned} H_0 : \frac{\sum_{n=1}^{N} |S_{rn}|^2}{\sigma_0^2} &\sim \chi^2(2N) \\ H_1 : \frac{\sum_{n=1}^{N} |S_{rn}|^2}{\sigma_1^2} &\sim \chi^2(2N) \end{aligned} \tag{32}$$

The values for σ_0^2 and σ_1^2 must be calculated in order to determine the decision regions. For Rayleigh clutter, σ_0^2 can be expressed as

$$\sigma_0^2 = \sum_{k=1}^{K} A_k^2 \sigma_{ck}^2 + \sigma_n^2 \sum_{k=1}^{K} A_k \tag{33}$$

where σ_{ck}^2 is the variance of the real component of the k^{th} clutter patch. In this calculation, the value for A_k is not in units of m^2, but is treated as a coefficient equal to the number of 1 m^2 sub-pixels which lie within each clutter patch. Since each 1 m^2 sub-pixel within the clutter patch is assigned the same value based upon a realization from the Rayleigh distribution with the appropriate σ_{ck} value, the variance is multiplied by a factor of A_k^2. The noise is also represented as a coefficient for a 1 m^2 sub-pixel, but each noise realization is independent, so the total variance due to the noise is the sum of the noise variances for each 1 m^2 sub-pixel in the resolution cell, which is the product of the noise coefficient and the total area of the resolution cell (which can be expressed as the sum of the areas of the individual clutter patches).

The area of the target displaces a portion of the clutter, so the appropriate changes are implemented to define σ_1^2 as

$$\sigma_1^2 = \sum_{k=1}^{K} (A_k - \epsilon_k)^2 \sigma_{ck}^2 + (A_t + A_{ov})^2 \sigma_t^2 + \sigma_n^2 \sum_{k=1}^{K} A_k \tag{34}$$

where σ_t^2 is the variance of the real component of the target return. The probability of false alarm (P_{fa}) represents the portion of the H_0 PDF which lies within the decision region for H_1. The probability of detection (P_d) is the portion of the H_1 PDF which

lies in the decision region for H_1. These can be expressed using integrals as

$$P_{fa} = \int_{\Gamma_1} p\left(\sum_{n=1}^{N} |S_{rn}|^2 \middle| H_0\right) \tag{35}$$

$$P_d = \int_{\Gamma_1} p\left(\sum_{n=1}^{N} |S_{rn}|^2 \middle| H_1\right) \tag{36}$$

where Γ_1 is the detection region for H_1, as calculated in Eq. (30) using the σ_0^2 and σ_1^2 values determined from Eq. (33) and Eq. (34). These integrals are taken over χ^2 distributions, so the result can be expressed in terms of the cumulative distribution function (CDF) for a χ^2 distribution, which is

$$P(\chi^2(\nu) < \gamma_k) = \frac{1}{\Gamma_F(\nu/2)}\, \gamma_f\left(\frac{\nu}{2}, \frac{\gamma_k}{2}\right) \tag{37}$$

where Γ_F signifies the Gamma function, γ_f is the lower incomplete gamma function, γ_k is the kth detection threshold, and ν is the number of degrees of freedom in the χ^2 distribution, which is $2N$ in this case.

3.2.4 Unknown Target Location.

If the target location is not known, then it is impossible to calculate σ_1^2 outright because the value of $\boldsymbol{\epsilon}$ is unknown, where $\boldsymbol{\epsilon} = [\epsilon_1, ..., \epsilon_K]^T$ is a vector representing the area of each clutter patch obstructed by the target or its shadow. The prior probability of $\boldsymbol{\epsilon}$, $p(\boldsymbol{\epsilon})$, must be paired with its corresponding value for σ_1^2. $p(\boldsymbol{\epsilon})$ can be calculated when the clutter layout of a resolution cell is previously known from land cover maps or overhead imagery.

The most concise solution to solve for $\boldsymbol{\epsilon}$ would be to find the maximum likelihood estimate (MLE). The MLE for $\boldsymbol{\epsilon}$ cannot be found directly since the parameter that can be solved for is σ_1^2. However, since $\boldsymbol{\epsilon}$ is multi-dimensional and σ_1^2 is a scalar,

solving for $\boldsymbol{\epsilon}$ using the estimate for σ_1^2 and Eq. (34) yields a multi-dimensional solution space; a single maximum likelihood estimate for $\boldsymbol{\epsilon}$ cannot be determined, so another approach must be taken.

If the target position is represented as a continuous value, as opposed to discretely, then the PDF for $p(\boldsymbol{\epsilon})$ is a mixture of probabilities and Dirac delta functions. This is because there exists a range of positions for which a target is entirely within a specific clutter patch, but one unique position for certain $\boldsymbol{\epsilon}$ values where the target is straddling multiple patches.

Taking these factors into consideration, it is more efficient to define a finite number of different positions at which the target could lie. $p(\boldsymbol{\epsilon})$ can then be expressed as the number of positions which correspond to a specific $\boldsymbol{\epsilon}$ value, compared to the total number of discrete target positions.

The Bayesian approach to a composite hypothesis test is the appropriate method of analysis, given that $\boldsymbol{\epsilon}$ has a defined prior probability which can be relayed into a prior probability for σ_1^2, $p(\sigma_1^2)$ [30]. H_1 is the decided-upon hypothesis if

$$\frac{p(|S_r|;H_1)}{p(|S_r|;H_0)} = \frac{\int p\left(|S_r|\middle|\sigma_1^2;H_1\right)p(\sigma_1^2)d\sigma_1^2}{\int p\left(|S_r|\middle|\sigma_0^2;H_0\right)p(\sigma_0^2)d\sigma_0^2} > \lambda \tag{38}$$

The value of σ_0^2 is deterministic and the probability mass function (PMF) on $p(\boldsymbol{\epsilon})$ is discrete, so Eq. (38) reduces to

$$\frac{\sum_{y=1}^{Y} p\left(|S_r|\middle|\sigma_{1y}^2;H_1\right)p(\sigma_{1y}^2)}{p(|S_r|;H_0)} > \lambda \tag{39}$$

where σ_{1y}^2 is the value for σ_1^2 for the y^{th} value of $\boldsymbol{\epsilon}$ and Y is the number of possible values for $\boldsymbol{\epsilon}$ in the discrete representation.

Therefore, the likelihood function is a weighted average of the individual likelihood functions for each target location based on the specific σ_1^2 value at each location (as

defined by $\boldsymbol{\epsilon}$ in Eq. (34)) and the probability of the target appearing in a location that yields the corresponding σ_1 value.

Eq. (34) shows that the calculation of σ_1^2 is quadratic in nature. This potentially yields a scenario in which $\sigma_1^2 > \sigma_0^2$ for one value of $\boldsymbol{\epsilon}$ but $\sigma_1^2 < \sigma_0^2$ for another value of $\boldsymbol{\epsilon}$. The resultant PDFs for the χ^2 hypothesis test from Eq. (32) in this case appear similar to Fig. 10. There are multiple thresholds (γ) in order to maximize the detection

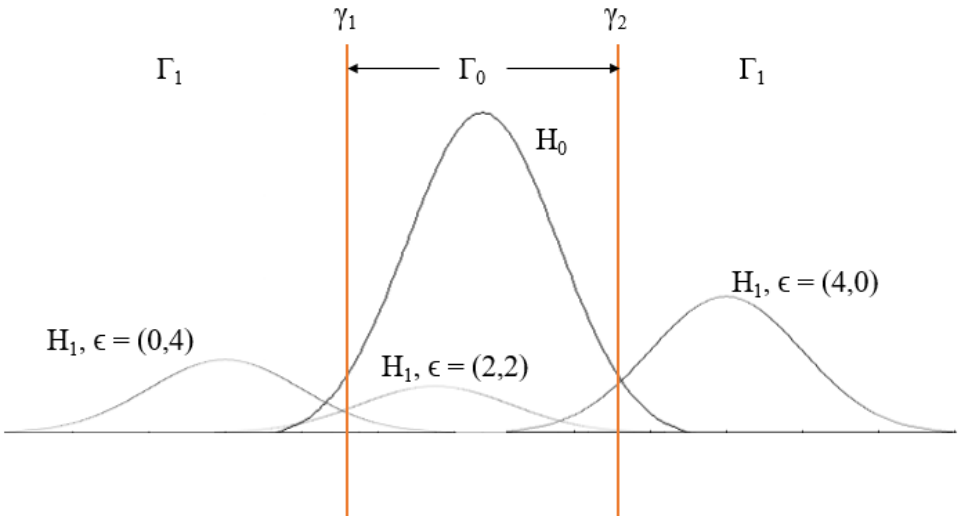

Figure 10: χ^2 PDFs for a detection scenario where the variance of the target-present cell may be greater or less than the variance of the cell with no target present. Two thresholds are used to decrease the false alarm rate and increase the probability of detection.

probability, accounting for the multi-modal PDF that can arise from combining three possible target locations. The thresholds serve as boundaries for the decision regions Γ_0 and Γ_1, where Γ_0 is the decision region for the target-absent hypothesis H_0. Due to the wide spreading of the multi-modal PDF, it is conceivable that Γ_1 consists of multiple non-contiguous sections. Each of the smaller PDFs represent a target-present scenario, and are scaled appropriately to their probability of occurrence. The prior probability of a target being present is necessary to appropriately scale the PDF representing σ_0. Once the PDFs are scaled, the probabilities of detection and false

alarm can be expressed as

$$P_{fa} = 1 - \int_{\gamma_1}^{\gamma_2} \chi^2_{2N} \left(\frac{S}{\sigma_0^2} \right) dS \tag{40}$$

$$P_d = \sum_{y=1}^{Y} p(\boldsymbol{\epsilon})_y \left(1 - \int_{\gamma_1}^{\gamma_2} \chi^2_{2N} \left(\frac{S}{\sigma_{1y}^2} \right) dS \right) \tag{41}$$

where Y is the total number of target locations that represent distinct $\boldsymbol{\epsilon}$ values, S is the test statistic $\sum_{n=1}^{N} |S_{rn}^2|$, $p(\boldsymbol{\epsilon})_y$ is the probability that the target appears in a location that yields the y^{th} value for $\boldsymbol{\epsilon}$, and σ_{1y} is the value of σ_1 for the value of $\boldsymbol{\epsilon}$ corresponding to the y^{th} target location. It is assumed that a threshold detector provides a ROC curve which is very close to the optimal result due to the shape of the χ^2-distributed sufficient statistics which all utilize the same number of degrees of freedom.

3.2.5 Resolving ROC Curves for Multiple-Threshold Scenarios.

The purpose of the ROC curve is to show the probability of detection as a function of the false-alarm rate. When only one threshold is used, there is only one possible position for the threshold at a given false-alarm rate since the integral defining the false-alarm rate is a function of the threshold position. Therefore, each false-alarm rate is in a one-to-one relationship with the probability of detection.

This is not true when two thresholds are used to define Γ_0, as seen in Fig. 10. There are a number of combinations for threshold positions γ_1 and γ_2 which will yield the same false-alarm rate. Between all of these pairs of thresholds, it is necessary to determine which generates the highest probability of detection.

In the case where there is only one threshold, the ROC curve is generated by sweeping the threshold through a large number of potential values, then calculating the corresponding P_{fa} and P_d, and connecting them with a smooth curve. When

there are two thresholds, combinations of two threshold values must be tested. A scatter plot is generated from many combinations of thresholds. The convex hull tool in MATLAB is used to include only the points which create a convex ROC curve, as shown in Fig. 11.

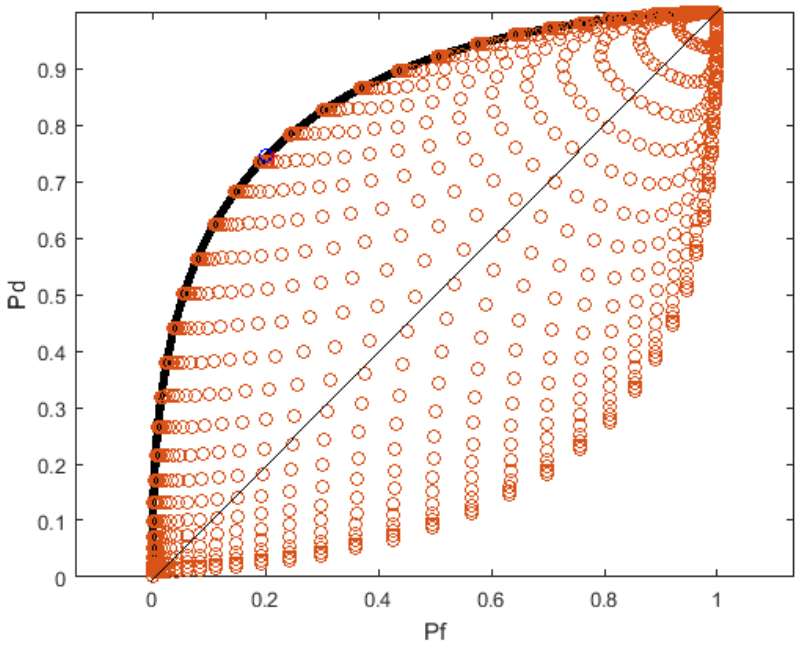

Figure 11: Each scatter point represents a γ_1 and γ_2 threshold pair; the curve represents the upper bound for P_d at each P_{fa} value. The line through the middle of the points is the random-guess line.

3.3 Position Estimation

Estimating the location of the target within the resolution cell can be performed by solving a multiple hypothesis detection problem where Y represents the number of possible values of $\boldsymbol{\epsilon}$. The detector can be used to pick which σ_1^2 value triggered the detection. Based upon the σ_1^2 value, the value of $\boldsymbol{\epsilon}$, which indicates the position of the target, can be extrapolated.

As discussed in Chapter 2, the multiple hypothesis detector relies on a cost matrix to minimize the risk of deciding incorrectly. As the number of considered locations increases, so does the size of the cost matrix, and therefore the computational complexity of the detection. When estimating the location of a resolution cell known to contain a target, either the entire target is within the same clutter patch, or the target straddles multiple clutter patches.

To utilize the locator, the assumption is made that the detector has already determined that there is a target present, so there is no need to consider the target-absent hypothesis H_0.

3.3.1 Hypotheses.

One simple estimation model for heterogeneous clutter may only test locations where the target is entirely within the same clutter patch. The hypothesis test for this set of locations would be

$$\begin{aligned} H_1 &: |S_r| = \text{clutter - reduced clutter 1} + \text{noise} + \text{target} + \text{shadow} \\ H_2 &: |S_r| = \text{clutter - reduced clutter 2} + \text{noise} + \text{target} + \text{shadow} \\ &\vdots \\ H_K &: |S_r| = \text{clutter - reduced clutter K} + \text{noise} + \text{target} + \text{shadow} \end{aligned} \tag{42}$$

Instead of listing the hypotheses in terms of the total return, they can also be expressed as hypotheses for the value of $\boldsymbol{\epsilon}$. The expression for the multiple hypotheses

with respect to $\boldsymbol{\epsilon}$ is

$$\begin{aligned} H_1 &: \boldsymbol{\epsilon} = [A_t + A_s, 0, ..., 0, 0]^T \\ H_2 &: \boldsymbol{\epsilon} = [0, A_t + A_s, 0, ..., 0]^T \\ &\vdots \\ H_K &: \boldsymbol{\epsilon} = [0, 0, ..., 0, A_t + A_s]^T \end{aligned} \tag{43}$$

Listing the hypotheses in this manner is useful because they can be tied to the prior probability of $\boldsymbol{\epsilon}$, which is determined by the geometry of the target and the layout of the clutter patches within the resolution cell. As with the detection problem, it is assumed that the target lies on lattice points and entirely within the resolution cell. Fig. 12 represents a scaling of the PDFs for each target location based upon the prior probabilities of the target locations and corresponding $\boldsymbol{\epsilon}$ values.

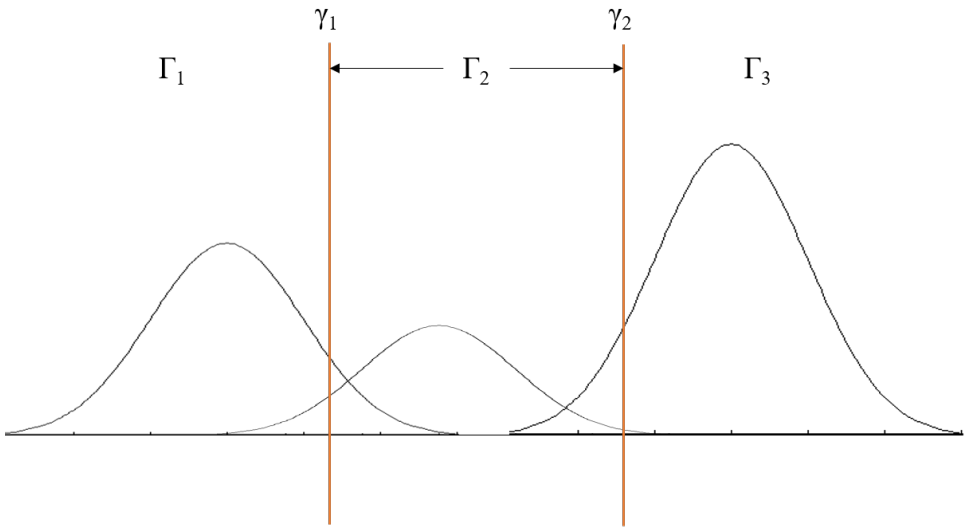

Figure 12: The threshold positions determine the decision regions for H_i and are placed at the values which reduce risk.

To create a more accurate position estimator, target positions can be considered which straddle multiple clutter patches. This will introduce additional hypotheses

where there are multiple non-zero elements of $\boldsymbol{\epsilon}$. The following hypotheses could be appended to the set from Eq. (43):

$$\begin{aligned} H_{K+1} &: \boldsymbol{\epsilon} = [0.5(A_t + A_s), 0.5(A_t + A_s), 0, ..., 0]^T \\ H_{K+2} &: \boldsymbol{\epsilon} = [0, 0.4(A_t + A_s), 0.6(A_t + A_s), ..., 0]^T \\ H_{K+3} &: \boldsymbol{\epsilon} = [0.25(A_t + A_s), 0.25(A_t + A_s), ..., 0, 0.5(A_t + A_s)]^T \\ &\vdots \\ H_Y &: \boldsymbol{\epsilon} = \dots \end{aligned} \tag{44}$$

Because, in reality, a target position is continuous rather than discrete, there are endless possibilities for the target positions and corresponding hypotheses that could be considered, so long as the constraint $\sum_{k=1}^{K} \epsilon_k = A_s + A_t$ holds. That is why this thesis will focus only on possible target locations whose boundaries are on lattice points. The purpose is to limit the number of hypotheses under consideration by discretizing the target location.

A confusion matrix must be used in order to adequately characterize the success of the locator. This experiment relies heavily on the prior probability of a target being present or absent, so it will be assumed that it is known that a target is present, and the task is to refine its location.

3.3.2 Risk Calculation.

The overall purpose of the position estimator should be to determine a location for the target with the least amount of error. This error can be expressed as risk, which also must be minimized in a multiple hypothesis detection test. The risk is equivalent to the expected error (in meters) for the location estimation.

The formula for risk is

$$\mathcal{R} = \sum_{i=1}^{M} \sum_{j=1}^{M} C_{ij} P[\text{pick } H_i | H_j \text{ true}] P[H_j] \tag{45}$$

where $\mathcal{R}$ is the detection risk and C_{ij} is the cost function for choosing H_i when H_j is the true hypothesis.

3.3.2.1 Cost Matrix.

In Fig. 3(b), if a target is located in clutter patch 1, there is a greater degree of error in deciding that the target is in clutter patch 3 as opposed to deciding that it is in clutter patch 2. When the resolution cell is comprised of large clutter patches, it is not always conceivable to determine the exact location of a detected target; the best possible outcome is to decide the $\boldsymbol{\epsilon}$ value which represents the area of obstructed clutter in each patch. If the detector decides that a target is located entirely within clutter patch 1, there exists a range of locations where the target could actually lie. One position to estimate for the target is the center of the clutter patch, because this reduces the expected location error for a correct decision.

Each cost matrix entry C_{ij} can be evaluated by calculating the expected error between the estimated position for H_i and each possible target position for H_j.

3.3.2.2 Prior Probability of H_j.

The prior probability of H_j can be expressed as the prior probabilities of the $\boldsymbol{\epsilon}$ values which correspond to each hypothesis.

3.3.2.3 Probability of Hypothesis Selection.

The $\boldsymbol{\epsilon}$ values used to define each of the Y hypotheses correspond to a σ_1^2 value, which can be used to build a PDF for the sufficient statistic derived in Section 3.2.3.

$Y-1$ thresholds are chosen to separate the Y χ^2 PDFs, designated as a vector $\boldsymbol{\gamma} = [\gamma_1, ...\gamma_{Y-1}]^T$. In order to bound each decision region by two thresholds, including at the upper and lower bounds, $\gamma_0 = 0$ and $\gamma_Y = \infty$ are included in each $\boldsymbol{\gamma}$ set.

Similar to the detection test, the threshold method is used because the χ^2-distributed sufficient statistic PDFs are not prone to yield irregular decision regions, so the interval method is an approximation of the optimal decision. As the number of target locations Y increases, so does the number of necessary thresholds to discriminate between each of the prospective positions. Generating a large value of Y, therefore, substantially increases the complexity of the simulation by requiring a large set of thresholds to be determined.

The interval between neighboring thresholds represents a decision region Γ_i for H_i. The value of i for each decision region is determined by sorting the σ_1^2 values for each hypothesis in ascending order; if $\sum_{n=1}^{N} |S_{rn}|^2$ is between γ_{z-1} and γ_z, the chosen hypothesis is the one with the z^{th}-largest σ_1^2 value.

$P(\text{pick } H_i|H_j)$ can be manipulated by selecting $\boldsymbol{\gamma}$ to minimize the risk of location error. For each $\boldsymbol{\gamma}$, $P(\text{pick } H_i|H_j)$ is calculated by calculating the integral for each χ^2 distribution (corresponding to H_j) within each decision region Γ_i, as

$$P(\text{pick } H_i|H_j) = \int_{\gamma_{u(i)-1}}^{\gamma_{u(i)}} \frac{(S/\sigma_{1j}^2)^{N-1} e^{-S/2\sigma_{1j}^2}}{2^N (N-1)!}\, dS \tag{46}$$

where $u(i)$ is the index of σ_{1i}^2 among the sorted σ_1^2 values for all hypotheses, S is the test statistic $\sum_{n=1}^{N} |S_{rn}|^2$, and σ_{1j} is the value of σ_1^2 for H_j.

For each set of $\boldsymbol{\gamma}$, $P(\text{pick } H_i|H_j)$ is calculated to evaluate $\mathcal{R}$. The values of $\boldsymbol{\gamma}$ are swept, and the $\boldsymbol{\gamma}$ which yields the lowest resultant risk is used in the multiple hypothesis detection test. The hypothesis that is chosen within the test corresponds to a σ_1^2 value, which in turn corresponds to a value for $\boldsymbol{\epsilon}$. The value for $\boldsymbol{\epsilon}$ then lends information as to the sub-pixel target location.

IV. Results and Analysis

The following chapter explores the techniques that were used in target detection and position estimation. The goal for the detection test is to develop a ROC curve to represent the detections and false alarms that are made by the detector given various sets of parameters. The objective of the estimation section is to reduce the positioning error of a target from what the error would be if the target is assumed to be at the center of the cell. Simulations are performed to verify that the theoretical results match experimental data.

4.1 Rayleigh Model Detection - 2 Clutter Types

The first model which will be analyzed is a Rayleigh-magnitude model for the clutter sections and target.

4.1.1 Parameter Setup.

The parameters will be varied throughout the simulation to observe their individual impact on the detection model, but the following are the initial baseline parameters:

- $R_{res} = 7$ m, $CR_{res} = 4$ m
- $A_1 = 16$ m^2, $A_2 = 12$ m^2, $A_t = 4$ m^2
- $\sigma_c^2 = (3, 6)$, $\sigma_t^2 = 20$, $\sigma_n^2 = 1$
- $v = 100$ m/s, $f_{PRF} = 10000$ Hz, $R = 100$ m, $Z = 1000$ m, $\theta = 0.10$ rad
- $\ell_R = 2$ m, $\ell_{CR} = 2$ m, $h = 1$ m

where ℓ_R and ℓ_{CR} are the dimensions of the target in range and cross-range, respectively.

The number of pulses received is

$$\begin{aligned} m &= \frac{f_{PRF}\theta R}{v} \\ &= 1000 \end{aligned} \tag{47}$$

Using the 2-pulse sub-aperture interleave method as described in Section 3.1.1.3, $N = 500$ sub-apertures can be formed. Refer to Fig. 13 for a visual layout of this cell. The target placement is not deterministic; it is demonstrated in Fig. 13 at a position of (4 m, 2 m), where the coordinates represent the range and cross-range, respectively, of the center of the upper-leftmost target sub-pixel. The collection is taken from a very high grazing angle, so there is assumed to be a negligible amount of shadow or target overlay in this model. The values used in this simulation are not based upon an actual measurement scenario but are realistic of a sensor platform.

4.1.2 Hypotheses.

As demonstrated in Chapter 3, the hypotheses for the detection test can be expressed in terms of the Rayleigh parameter which defines the distribution for the magnitude of the return. These hypotheses can be written as

$$\begin{aligned} H_0 &: |S_r| \sim \text{Rayleigh}(\sigma_0) \\ H_1 &: |S_r| \sim \text{Rayleigh}(\sigma_1) \end{aligned} \tag{48}$$

The values for σ_0 and σ_1 must be calculated in order to determine the decision region. Using the given parameters, the real-component variance for received power with no

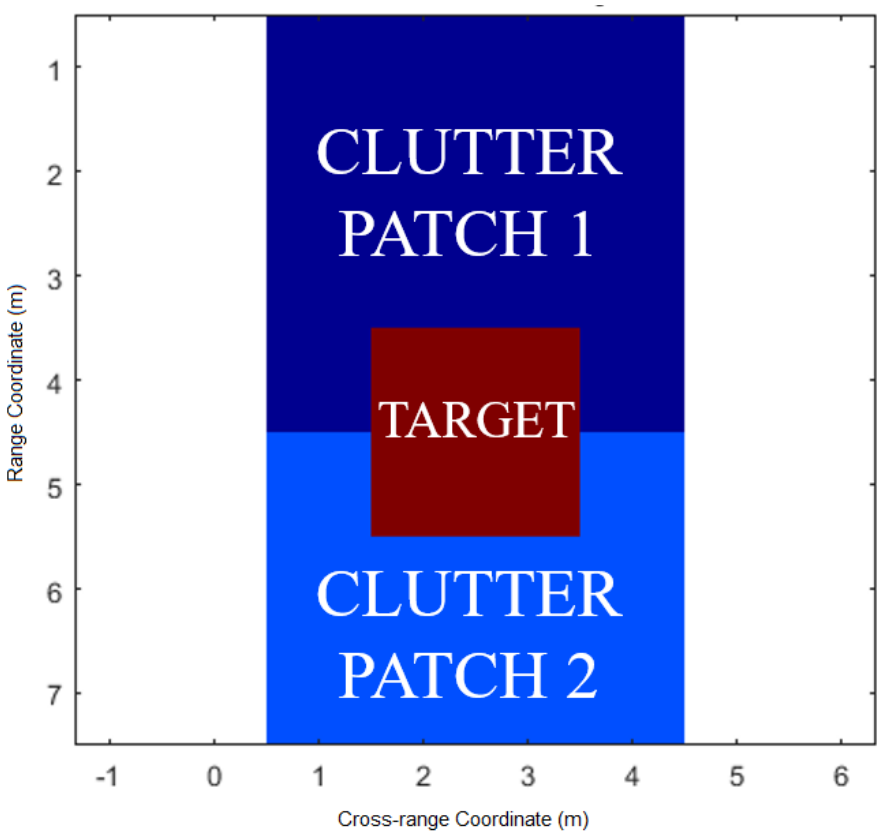

Figure 13: Resolution cell which is 4 meters in cross-range and 7 meters in range. The target position is 3 meters in range and 1 meter in cross-range (distance of top-left target corner from top-left resolution cell corner).

target present is

$$\begin{aligned}\sigma_0^2 &= A_1^2\sigma_{c1}^2 + A_2^2\sigma_{c2}^2 + (A_1 + A_2)\sigma_n^2 \\ &= (256)(3) + (144)(6) + (28)(1) \\ &= 1660 \end{aligned} \tag{49}$$

The value for σ_1^2 is dependent on the value of $\boldsymbol{\epsilon}$. Because of the constraint that $\sum_{k=1}^{K} \epsilon_k = A_t + A_s$, $A_t = 4$, $A_s = 0$, and there are only two components of the vector

$\boldsymbol{\epsilon}$, ϵ_2 can be expressed as $4 - \epsilon_1$. Given this substitution, σ_1^2 can be computed as

$$\begin{aligned}\sigma_1^2 &= (A_1 - \epsilon_1)^2\sigma_{c1}^2 + (A_2 - \epsilon_2)^2\sigma_{c2}^2 + (A_t + A_{ov})^2\sigma_t^2 + (A_1 + A_2)\sigma_n^2 \\ &= 3(16 - \epsilon_1)^2 + 6(12 - (4 - \epsilon_1))^2 + (16)(20) + (28)(1) \\ &= 1500 + 9\epsilon_1^2 \end{aligned} \tag{50}$$

The prior probability of $\boldsymbol{\epsilon}$ is used to create a distribution for σ_1^2. Since there are no clutter boundaries in the cross-range dimension, the range-dimension coordinate of the target will be the sole factor in determining $\boldsymbol{\epsilon}$.

There are 3 range coordinates (1 m, 2 m, 3 m) for which the target is entirely in clutter patch 1. In this case, $\boldsymbol{\epsilon} = [4, 0]^T$, since 4 m^2 of clutter are obstructed in clutter patch 1, and there is no clutter obstructed from patch 2. At the range coordinate of 4 m, the target straddles clutter patches 1 and 2, obstructing 2 m^2 of clutter from each patch; therefore $\boldsymbol{\epsilon} = [2, 2]^T$. For range coordinates 5 m and 6 m, the target is entirely in clutter patch 2; $\boldsymbol{\epsilon} = [0, 4]^T$. The target cannot be placed at a range of 7 m because it would extend beyond the boundary of the resolution cell, which is not allowed under the previously-placed constraints.

The number of positions which yield specific $\boldsymbol{\epsilon}$ values can be used to generate a PMF for $\boldsymbol{\epsilon}$, which is

$$p(\boldsymbol{\epsilon}) = \begin{cases} 1/3, & \boldsymbol{\epsilon} = [0, 4]^T \\ 1/6, & \boldsymbol{\epsilon} = [2, 2]^T \\ 1/2, & \boldsymbol{\epsilon} = [4, 0]^T \end{cases} \tag{51}$$

This PMF can then be used to create a PMF for σ_1^2, as

$$p(\sigma_1^2) = \begin{cases} 1/3, & \sigma_1^2 = 1500 \\ 1/6, & \sigma_1^2 = 1536 \\ 1/2, & \sigma_1^2 = 1644 \end{cases} \tag{52}$$

4.1.3 Detection and False Alarm Statistics.

The threshold can be used to compute the probability of false alarm (P_{fa}) and probability of detection (P_d)

$$P_{fa} = \int_{\Gamma_1} p\left(\sum_{n=1}^{N} (|S_{rn}|^2) \middle| H_0 \right) \tag{53}$$

$$P_d = \int_{\Gamma_1} p\left(\sum_{n=1}^{N} (|S_{rn}|^2) \middle| H_1 \right) \tag{54}$$

P_{fa} and P_d are integrals of χ^2 functions with $2N$ degrees of freedom. It is acceptable in this case to use only one threshold since there is no upper bound for the region where σ_0 is more likely than σ_1. This is not always true; the parameters used in this simulation provide for this condition. Limiting the detection region to one boundary will make it substantially easier to define the false-alarm rate. Initially, P_{fa} will be set at 0.1, but the ROC curve will show the probability of detection at any false-alarm rate by sweeping the detection threshold γ over a wide range of values.

The probability of false alarm defines the value of the threshold γ, which can be

calculated as

$$\begin{aligned} P_{fa} &= p(\chi^2(1000) > \frac{\gamma}{\sigma_0^2}) \\ 0.1 &= p(\chi^2(1000) > \frac{\gamma}{1660}) \\ \gamma &= 1660(\chi^2_{0.1}(1000))^{-1} \\ &= 1.57 \times 10^6 \end{aligned} \tag{55}$$

P_d can then be calculated using the threshold γ. The probability of detection is

$$\begin{aligned} P_d &= \sum_{k=1}^{K} p(\sigma_1 = \sigma_{1k}) p\left(\chi^2(1000) > \frac{\gamma}{\sigma_{1k}^2}\right) \\ &= \left(\frac{1}{3}\right) p\left(\chi^2(1000) > \frac{1.57 \times 10^6}{1500}\right) + \left(\frac{1}{6}\right) p\left(\chi^2(1000) > \frac{1.57 \times 10^6}{1536}\right) \\ &+ \left(\frac{1}{2}\right) p\left(\chi^2(1000) > \frac{1.57 \times 10^6}{1644}\right) \\ &= \frac{1}{3}(.8362) + \frac{1}{6}(.6711) + \frac{1}{2}(.1426) \\ &= 0.4619 \end{aligned} \tag{56}$$

Fig. 14 shows the ROC curve for the previous simulation. The 10% false-alarm rate corresponds to the 46.19% detection probability as calculated in Eq. (56). The next section explores how this ROC curve changes along with specific parameters.

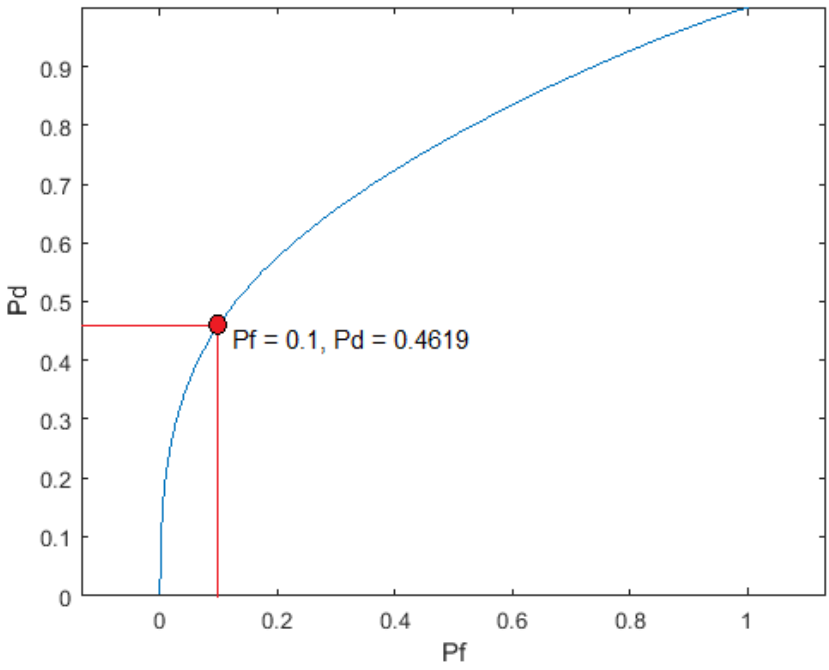

Figure 14: ROC curve for initial experiment parameters - clutter with Rayleigh magnitude in resolution cell with two clutter types.

4.1.4 Effects of Modifying Parameters.

One of the aims of this research is to determine the minimum conditions required to achieve sufficient detection in a low-resolution scenario. Thus, it is important to study the effects of changing the key parameters in the simulation.

4.1.4.1 Target Size.

Intuitively, a target which is physically larger in area (irrespective to the reflectivity of its material) should be easier to detect, but that is not always the case. In the previous example, σ_1^2 was smaller than σ_0^2, and the distributions varied enough that there was a discernible distinction between the ROC curve and a random guess. As the area of the target increases from the baseline example, so do the values of σ_1^2.

The distributions for H_0 and H_1 approach each other, and the probability of error increases up to the point where σ_0^2 becomes incredibly close to σ_1^2. However, as the target size continues to increase beyond this point, σ_1^2 grows larger than σ_0^2, and the hypothesis distributions begin to separate again. If the target size is decreased, σ_1^2 decreases (to a point) and separates further from σ_0^2. As the target size approaches zero, the value of σ_1^2 approaches σ_0^2. So, detector accuracy is somewhat of a third-order function based upon target size. Fig. 15(a) and Fig. 15(b) show the ROC curves as a function of ℓ_R (ℓ_{CR} is fixed at the length specified in each figure).

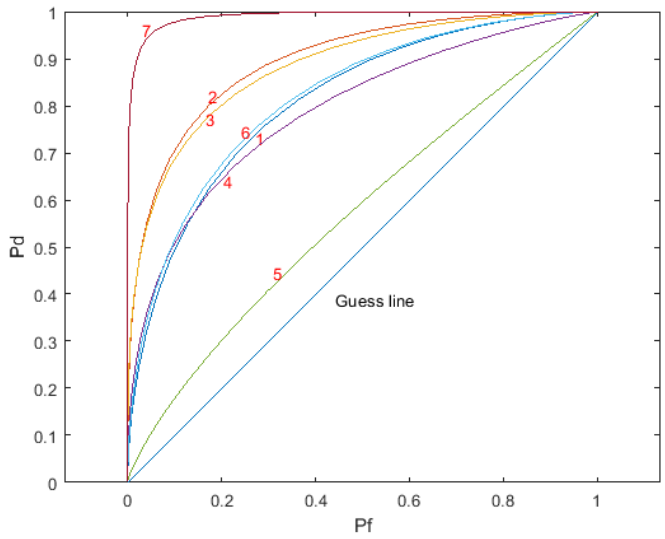

(a) ℓ_{CR} fixed at 1 meter

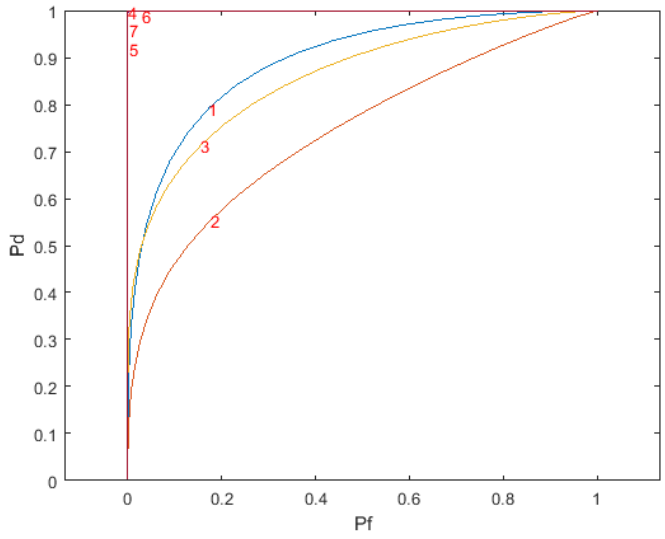

(b) ℓ_{CR} fixed at 2 meters

Figure 15: Effect of target size on detection accuracy - each subfigure is labeled with its ℓ_{CR}, each curve is labeled with its ℓ_R. A larger target is generally more detectable, but there are specific sizes of targets which yield σ_1^2 that make the cell indistinguishable from the target-absent case.

4.1.4.2 Noise.

In a high-noise environment, the large noise variance contributes to both σ_1^2 and σ_0^2. The high noise level diminishes the $\frac{\sigma_1^2}{\sigma_0^2}$ ratio and moves the distributions relatively closer together, making detection less likely. The result for varying levels of σ_n^2 (as denoted by the labels on each curve) and a target with $\ell_R = 3$ m, $\ell_{CR} = 2$ m is shown in Fig. 16.

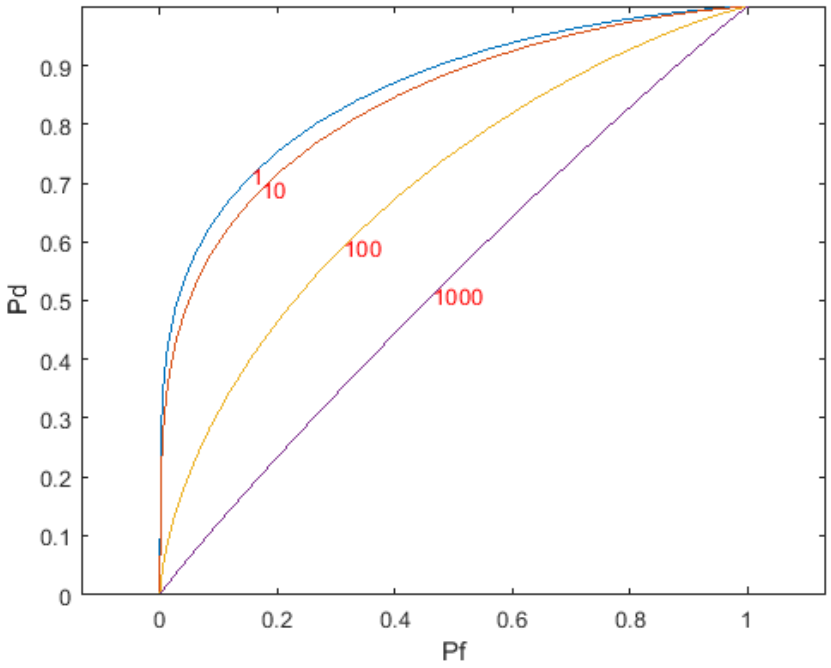

Figure 16: Effect of increased noise level on ROC curves - label indicates σ_n^2.

4.1.4.3 Target Reflectivity.

A target which is more reflective would seem to be easier to detect. Similar to the case of varying target sizes, this is not necessarily so. Fig. 17 shows the ROC curves of a 2 m $\times$ 2 m target with the reflectivity variances indicated by the plot markers.

Fig. 18(a) shows the detection accuracy at the optimal operating point for each

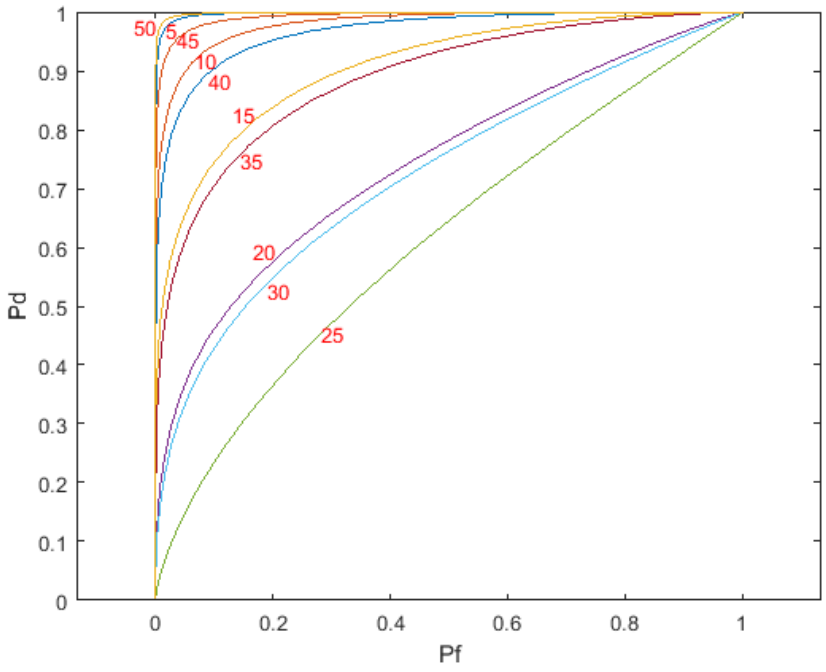

Figure 17: ROC curves for a 2m x 2m target by σ_t^2 values.

ROC curve. The minimum occurs at $\sigma_t = 25$, which is the value at which σ_1 closest approaches σ_0 and the decision is little better a random guess (58.62% accuracy). As the reflectivity decreases down to 0, the accuracy rate continues to increase; a large portion of the resolution cell reflecting very little signal is just as detectable as a portion reflecting a high signal amongst clutter. Fig. 18(b) demonstrates why there is a dip in detection performance at a particular value for σ_t^2. The value of σ_1^2 is linearly dependent on the value for σ_t^2. As σ_t^2 increases, the values for σ_1^2 (the three increasing functions) approach σ_0^2 (the constant function) and their distributions become less discernible. As σ_t^2 continues to increase beyond this region, the distributions once again become more distinct and the accuracy rate improves.

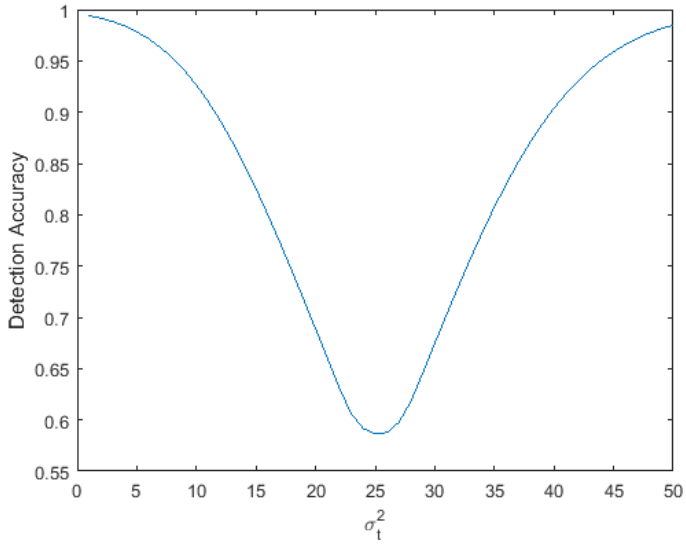

(a) Maximum detection accuracy ($\frac{P_d+(1-P_{fa})}{2}$) as a function of σ_t^2

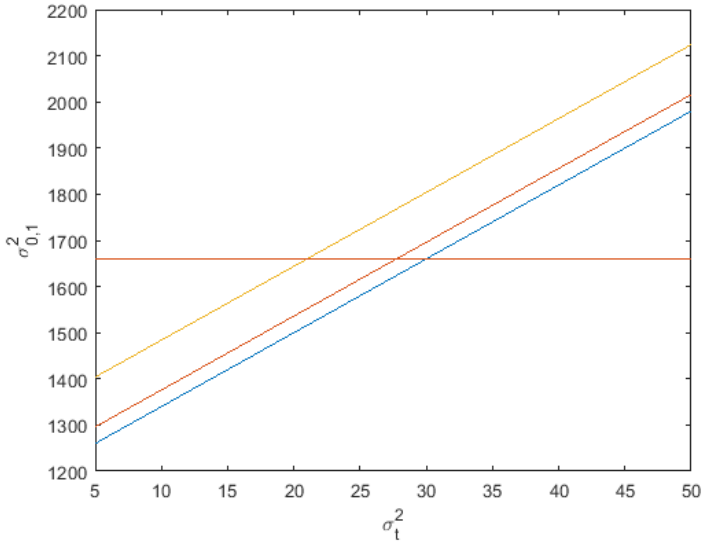

(b) Values of σ_1^2 (increasing functions) and σ_0^2 (constant function) as a function of σ_t^2

Figure 18: As the value of σ_t^2 grows, the possible values of σ_1^2 increase linearly. The region where the values of σ_0^2 and σ_1^2 are close together is where the detection accuracy is minimized. This occurs at $\sigma_t^2 = 25$.

4.1.4.4 Pulses Collected.

Another way to increase the probability of detection is to collect more data. When more pulses are collected, more 2-pulse sub-apertures can be created. Fig. 19 shows the ROC curves for a 3 meter by 2 meter target ($\sigma_t^2 = 20$) varying the number of sub-apertures available for data analysis. Increasing the size of the dataset will always improve detection accuracy, as also shown in Fig. 20.

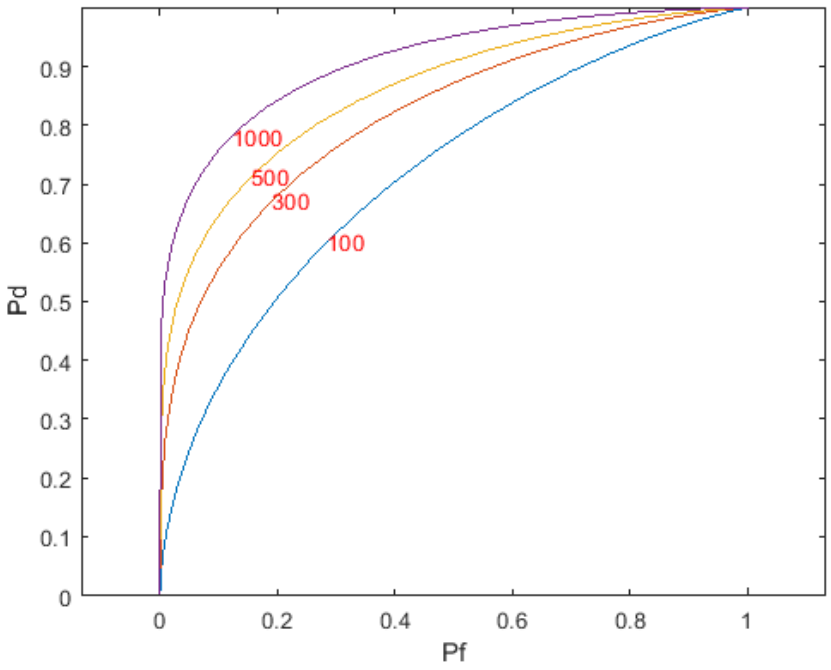

Figure 19: ROC curves for a resolution cell containing a 3m x 2m target by number of sub-apertures created.

4.1.4.5 Sub-apertures.

Fig. 19 concludes that in a Rayleigh scenario, it is typically not advisable to split the main aperture of signal collection into sub-apertures of greater than 2 pulses. However, this is contingent upon the assumption that the sub-apertures are i.i.d.. The maximum number of sub-apertures must be determined on a case-by-case basis;

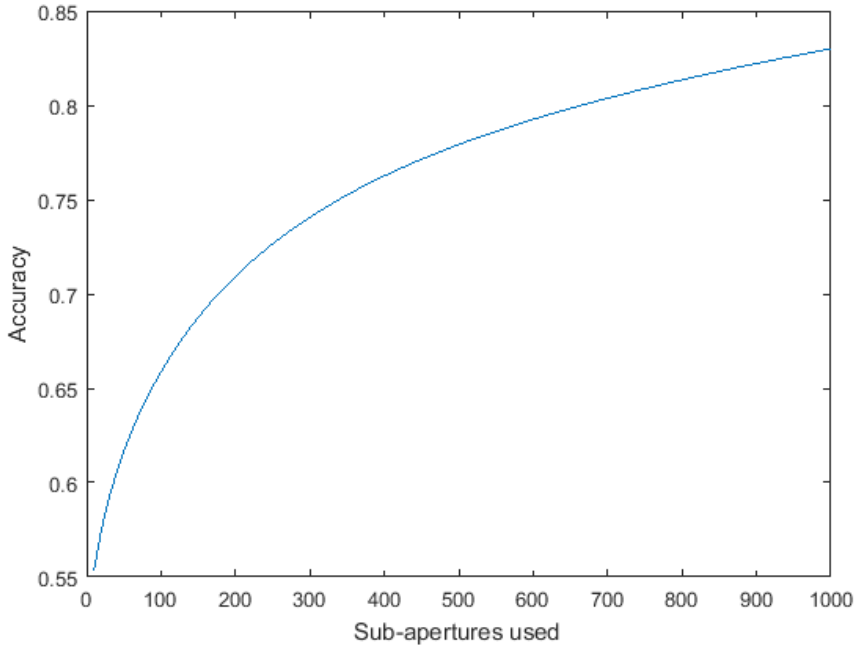

Figure 20: Accuracy rate ($\frac{P_d+(1-P_{fa})}{2}$) based on the number of collected sub-apertures for a cell with a 3m x 2m target. The accuracy of the detector will always increase when more sub-apertures are used. If more than 2 pulses are used per sub-aperture, the results remain the same but the scene size is more expansive.

it is always advisable to use the maximum in order to produce the highest probability of detection.

4.1.5 Comparison to Simulated Data.

In the previous sections, the ROC curves were generated based upon the expected distribution of the resolution cell given specific parameters. In this section, the resolution cell is simulated over a large number of trials to confirm that the simulation setup is proper, comparing the detection decision (driven by the test statistic) to the true target status. The output of the detector D will either be a 0 (no target present) or a 1 (target present). In simulation, the simulated ROC curve is compared to the theoretical ROC curve to assure that the simulation performs as expected.

For an simulation consisting of J trials, the simulated probability of detection p_d and probability of false alarm p_{fa} will be calculated as defined below:

$$p_d = \frac{\sum_{j=1}^{J} D_j T_j}{\sum_{j=1}^{J} T_j} \tag{57}$$

$$p_{fa} = \frac{\sum_{j=1}^{J} (1 - D_j) T_j}{J - \sum_{j=1}^{J} T_j} \tag{58}$$

where T represents the true target status (0 = not present, 1 = present)

4.1.5.1 Setting the Scene.

In the first section of the simulation, the scene is created by simulating values for each of the clutter sections. The simulated values are drawn from the appropriate complex Gaussian distributions.

4.1.5.2 Target Placement.

A target is, at random, either added to the resolution cell or omitted. The probability of placing a target on the cell is 50%. The upper-left corner of the target (relative to the MATLAB figure output) is randomly placed on a lattice point such that the entire target fits within the resolution cell. Return values are generated with respect to the characteristics of the target; those new values replace the clutter.

4.1.5.3 Collection.

For each sub-aperture, the radar will receive a complex value that represents the sum of all scatterers. This is the only information available to the processor; the individual phases and magnitudes of each clutter or target section are modeled

within MATLAB to create a cumulative return, but are not individually used in the detection decision process.

4.1.5.4 Processing and Decision.

The collected values for each pulse are combined to build the sufficient statistic. In this case, this is the sum of squares of the magnitude of each return. The appropriate decision is made depending on which region the test statistic falls within. The decision regions are pre-determined from the theoretical portion of the simulation; they are generated from the thresholds that yield the greatest detection accuracy. If a target is present and the detector correctly determines so, the number of detections is incremented. If no target is present but the decision is made that a target is present, then the number of false alarms is incremented.

4.1.5.5 Repetition.

This process is repeated over a large series of trials ($J = 1000$), and at the end, the number of false alarms is divided by the number of trials in which no target was added to the cell. This represents the p_{fa} for the simulation. Likewise, p_d is calculated by dividing the number of detections by the number of trials in which a target was added.

Because the simulation inserts a target half of the time, the detection equation will assume equal costs and priors between H_0 and H_1. Therefore, the goal is to get the detector to choose correctly as often as possible, maximizing $\frac{P_d+(1-P_{fa})}{2}$. The threshold, derived from the theoretical results, is set to optimize this metric.

Table 2 shows several select scenarios, comparing the theoretical accuracy with the simulated accuracy.

Table 2: Observed results for simulations - key parameters were varied to measure success across multiple target scenarios. P indicates a theoretical probability whereas p denotes an experimentally calculated probability

ℓ_R	ℓ_{CR}	σ_t^2	σ_n^2	N	P_{fa}	p_{fa}	P_d	p_d
3	2	20	1	500	0.1556	0.1629	0.7139	0.7210
2	2	25	1	500	0.2816	0.2505	0.4540	0.4352
7	1	20	1	500	0.0469	0.0366	0.9502	0.9508
5	2	25	1	50	0.0084	0.0082	0.9891	0.9883
2	4	20	100	500	0.4845	0.5039	0.5035	0.5041
2	4	20	10	100	0.2491	0.2455	0.7181	0.7232

4.1.5.6 Confirmation of Results.

A binomial test can be used to confirm that the simulated data matches the theoretical expectation as some of the results exhibit a fairly wide differential between the observed and expected values. In the case of the 2nd simulation in Table 2, it is difficult to tell whether the p_{fa} of 25.05% is close enough to the theoretical value of 28.16%. The binomial test can assign a p-value to the probability of occurrence for the >3% discrepancy.

$$CDF = \sum_{i=0}^{F_A} \binom{J_0}{i} \cdot p^i q^{J_0 - i}$$

where J_0 is the number of trials without a target present, F_A is the number of false alarms in the simulation, $p = p_{fa}$, and $q = 1 - p$ [31].

$$CDF = \sum_{i=0}^{121} \binom{493}{i} \cdot (0.2816)^i (0.7184)^{493-i} \tag{59}$$

$$= 0.0400 \tag{60}$$

The two-tailed p-value is double this result, or 0.08, which is generally regarded as acceptable, especially when it is the lowest p-value among 12 results.

4.2 Rayleigh Model Estimation - 2 Clutter Types

If the target identification process ends at detection, the only information regarding the target location is that it is somewhere within the resolution cell. Since the σ_1^2 statistic varies with $\boldsymbol{\epsilon}$, which corresponds to the position of the target within the cell, it is possible to leverage this difference to distinguish between the possible target locations.

4.2.1 Setup.

Let it be assumed that the position estimation procedure only takes place if the detector has already determined that there is a target present. Because of this, there is no need to consider H_0 in the set of hypotheses. Beginning with the same initial parameters as in the detection piece, the following set of hypotheses are tested:

$$\begin{aligned} H_1 &: \boldsymbol{\epsilon} = [0,4]^T \text{ (target in clutter region 2)} \\ H_2 &: \boldsymbol{\epsilon} = [2,2]^T \text{ (target in clutter regions 1 and 2)} \\ H_3 &: \boldsymbol{\epsilon} = [4,0]^T \text{ (target in clutter region 1)} \end{aligned} \tag{61}$$

4.2.2 Minimizing Risk.

The objective of a multiple hypothesis detection scheme is to minimize the risk of error. The error, in this case, is the discrepancy between the actual target location and the estimated location. If no estimation were to be conducted, then the target location, in order to reduce error, would be placed at the center of the resolution cell as shown in Fig. 21. If the proper value of $\boldsymbol{\epsilon}$ can be determined, then the estimated location for the target is refined, as shown in Fig. 22. From this point, it is straightforward to calculate a cost matrix which characterizes the average error when H_i is predicted and H_j is the true hypothesis. To simplify matters, only the

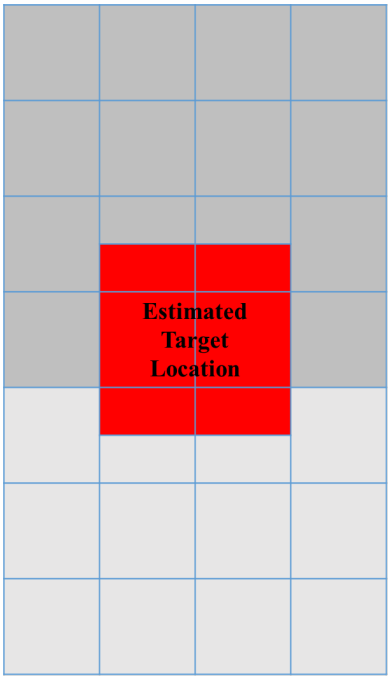

Figure 21: If the location of the target is uniformly distributed across the cell, placing it in the center of the resolution cell yields the lowest average error. The shades represent differing clutter profiles.

range error will be considered in this case (since the cross-range dimension contains no clutter boundaries and the cross-range within the cell is indiscriminable) and the edges of the target will be lattice points. This means that, for a target with $\ell_R = 2$, there are six possible range coordinates: [1 m, 2 m, 3 m, 4 m, 5 m, 6 m]. The average ranging error if the target is estimated at 3.5 meters is:

$$\frac{|1-3.5|+|2-3.5|+|3-3.5|+|4-3.5|+|5-3.5|+|6-3.5|}{6} = 1.5 \text{ meters}$$

The objective is to reduce that error using the following formula for risk:

$$\mathcal{R} = \sum_{i=1}^{M}\sum_{j=1}^{M} C_{ij} P[\text{pick } H_i | H_j \text{ true}] P[H_j] \tag{62}$$

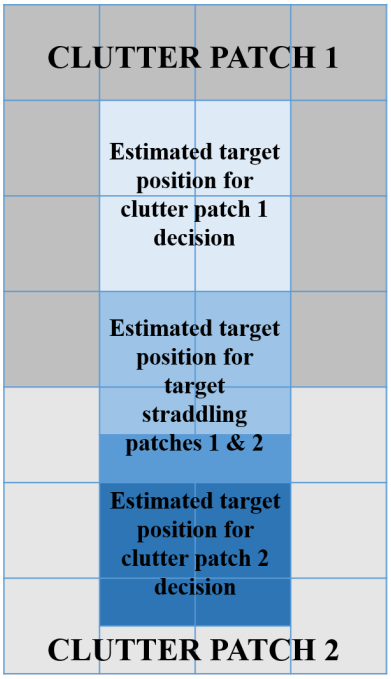

Figure 22: If the location of the target is uniformly distributed across the clutter region in which it is determined to lie, placing it in the center of the clutter region yields the lowest average error for a correct decision.

There are three components to Eq. (62): the cost matrix, the prior probability of P_j, and the probability of selecting H_i when H_j is true.

4.2.2.1 Cost Matrix.

If the target lies entirely in clutter patch 2 (H_1), it has two possible range coordinates (5 m, 6 m). If the target is estimated to be at 5.5 m, then the average error for predicting correctly is 0.5 m. A similar procedure can be used for all true and guess hypotheses to build a cost matrix:

$$C = \begin{bmatrix} 1/2 & 3/2 & 7/2 \\ 3/2 & 0 & 2 \\ 7/2 & 2 & 2/3 \end{bmatrix} \tag{63}$$

4.2.2.2 Prior Probability of H_j.

There are six possible range coordinates for the target. Two of these lie entirely within clutter section 2: [5 m,6 m]. Therefore, $P(H_1) = 1/3$. Likewise, there is only one location which straddles clutter sections 1 and 2 and yields an $\boldsymbol{\epsilon}$ value of (2,2), so $P(H_2) = 1/6$. The remaining target locations are all within clutter section 1; $P(H_3) = 1/2$.

4.2.2.3 Hypothesis Selection Probability.

The PDFs for the test statistic $\left(\sum_{n=1}^{N} |S_{rn}|^2\right)$ corresponding to each possible σ_1^2 value are χ^2 distributions, as determined in Section 3.2.3. These χ^2-distributed PDFs are shown in Fig. 23 and are denoted by $H_1,\ H_2,$ and H_3. The key component that must be controlled in order to reduce the overall risk is the location of each of the thresholds that determine the detection regions; the cost and prior probability of H_j are fixed. In simulation, an efficient way to pick the proper thresholds is to generate a bank of threshold combinations, then calculate the risk for each and select the thresholds which produce the minimum risk. Fig. 23 shows where the thresholds are placed such that the risk is minimized. There exists a detection region for H_2 despite that it is not the most likely hypothesis under any circumstance. This is due to the weighting of the cost function which carries less penalty for an incorrect decision if that decision is to choose H_2.

If there were more possible values for $\boldsymbol{\epsilon}$, then more thresholds would also be required. This adds to the simulation complexity as another dimension is added to the search space for the ideal set of thresholds. A similar figure for thresholds is shown in Fig. 24, where $\ell_R = 3$ so there are 4 possible $\boldsymbol{\epsilon}$ values instead of 3, requiring 3 thresholds.

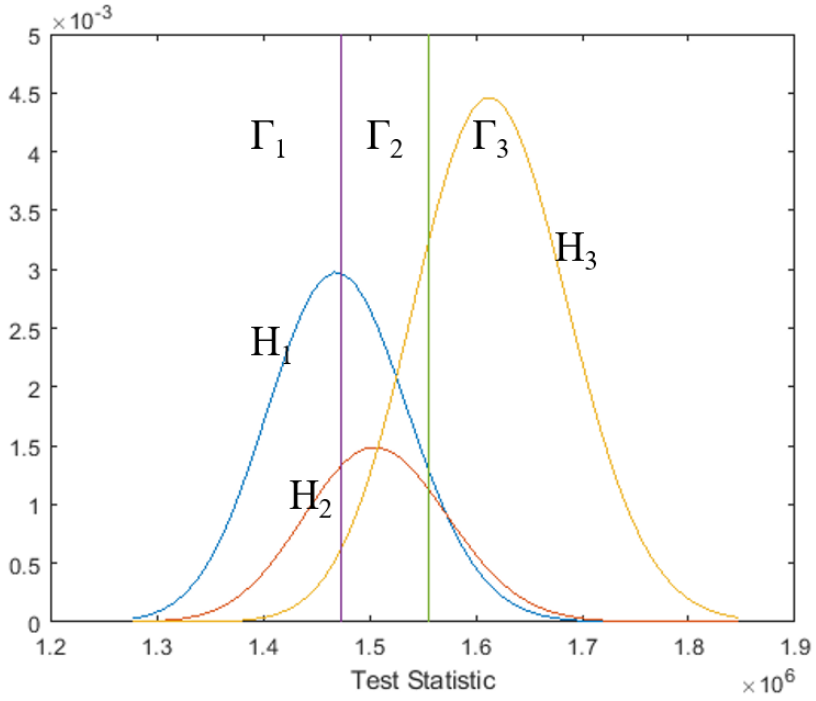

Figure 23: The threshold positions are chosen from a bank of values to minimize the risk in the experiment given the costs and priors previously calculated.

4.2.3 Confusion Matrix.

The purpose of the confusion matrix is to characterize how often a particular decision is reached given the true hypothesis. Table 3 shows the expected proportion of guesses for each hypothesis (by column) when a given hypothesis (by row) is true.

Table 3: Theoretical confusion matrix for test statistic PDFs in Fig. 23; the column represents the guess hypothesis and the row represents the truth hypothesis.

	H_1	H_2	H_3
H_1	0.5028	0.4104	0.0868
H_2	0.3011	0.4932	0.2056
H_3	0.0221	0.2202	0.7576

A second confusion matrix was created to test simulated results to the theoretical confusion matrix; it is shown in Table 4.

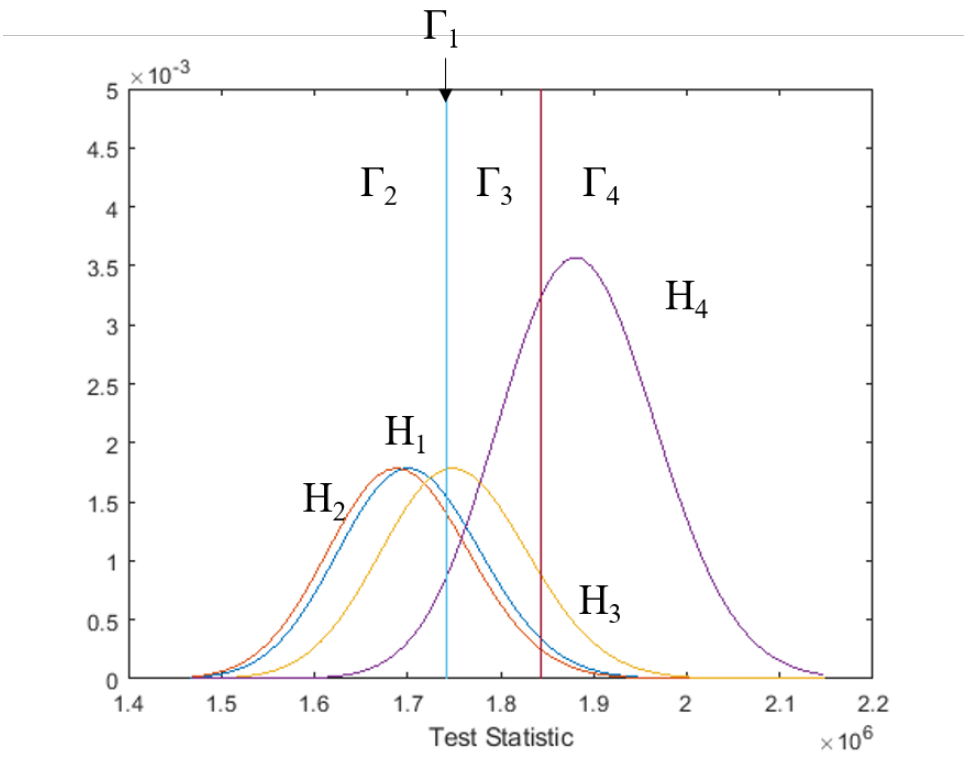

Figure 24: The threshold positions for $Y = 4$ are chosen in a similar manner as Fig. 23. Γ_1 is very small because H_1 is hardly distinguishable from H_2 and the penalty for incorrectly guessing H_1 is larger since it is farther from the center of the resolution cell.

4.2.4 Results.

The results were taken for targets of varying sizes and reflectivities to assess the robustness of this estimator. In every case, the estimator significantly reduced the amount of ranging error compared to using the cell center as a position estimate. Table 5 shows the different error values, in meters, for various sets of parameters, including target size (ℓ_R and ℓ_{CR}), target reflectivity (σ_t^2), noise factor (σ_n^2), and the number of sub-apertures used (N). The theoretical error is the minimum risk calculated from Eq. (62) by testing a large number of threshold sets. The observed error is the average error between the range of a simulated target and the range predicted by the detector. The no-estimate error is the expected ranging error between

Table 4: Simulated confusion matrix for test statistic PDFs in Fig. 23. - the proportions are similar to Table 3.

	H_1	H_2	H_3
H_1	0.5582	0.3343	0.1075
H_2	0.3444	0.4503	0.2053
H_3	0.0156	0.1984	0.7860

a simulated target and the center of the resolution cell. The effects of changing the target and radar parameters are discussed in the following subsections.

Table 5: Simulated results for position estimation simulations - key parameters were varied to measure success across multiple target scenarios. The error figures include theoretical, observed, and no estimation (target is always placed in the center of the resolution cell).

ℓ_R	ℓ_{CR}	σ_t^2	σ_n^2	N	Error (theo.)	Error (obs.)	Error (no est.)
2	2	20	1	500	1.046	1.020	1.5
2	2	20	0.01	500	1.039	1.005	1.5
2	2	20	10	500	1.407	1.355	1.5
2	2	40	1	500	1.136	1.130	1.5
2	2	100	1	500	1.302	1.270	1.5
2	2	5	1	500	0.964	0.980	1.5
3	3	20	1	500	0.875	0.888	1.2
4	2	20	1	500	0.604	0.585	1.0
2	2	20	1	100	1.361	1.370	1.5
2	2	20	1	1000	0.873	0.856	1.5
3	3	20	1	200	1.023	1.055	1.2

4.2.4.1 Target Size.

If the size of the target is increased, there is less error when no estimation is performed because there is a smaller range of freedom within the resolution cell for the large target. The resultant position estimation is also, then, finer than a smaller target.

4.2.4.2 Target Reflectivity.

Perhaps counter-intuitively, the position error of the target tends to increase as its reflectivity increases. The key to differentiating between which clutter types the target occupies is having relatively distinct clutter reflectivities. A more radiant target makes the clutter variances relatively small and indistinguishable, so the performance is better for less-reflective targets.

4.2.4.3 Noise Factor.

There is not a considerable gain in estimation accuracy when σ_n^2 decreases from 1 to 0.01, but the error significantly increases when σ_n^2 is changed from 1 to 10. Once the noise level is sufficiently small that it does not dwarf the signal return, the gains in benefit of enhanced position estimation are negligible.

4.2.4.4 Sub-apertures Utilized.

If fewer sub-apertures are used, the χ^2 distributions which make up the PDFs for the test statistic utilize fewer degrees of freedom and therefore overlap more and are less distinguishable. Estimation performance degrades as the number of sub-apertures (which is a byproduct of the number of received pulses) decreases.

4.2.4.5 Further Refining Location Estimates.

The error could be further reduced if the estimated positions for the target were modified. For example, if the estimator decides that the target is entirely in clutter patch 1, it is placed at a range coordinate of 2 meters. This minimizes the error for a correct decision. However, moving the predicted target placement closer to the center of the cell would decrease the cost of an incorrect decision. Doing this would change the cost matrix, which would in turn change the thresholds, which would modify the

minimum attainable risk. In order to reduce the number of variable components in this study, this scenario was not thoroughly investigated.

4.3 Rayleigh Model - 4 Clutter Types

The next case to consider is one in which there are more than two clutter types within the resolution cell and the target casts a shadow along with clutter overlap due to its height. The challenges associated with this model include characterizing the probability of $\boldsymbol{\epsilon}$ and determining the extent of the target shadow and overlap. Because of all of these variables, it is more cumbersome to generalize closed forms for the detection and estimation formulas. Therefore, any results henceforth will be conducted on a per-scenario basis; the effects of changing any parameters can be gleaned from the previous section.

4.3.1 Experiment Parameters.

One potential cause of a more heterogeneous resolution cell is poor cross-range resolution. This would most likely be due to a limited sub-aperture support angle. In this experiment, the cross-range resolution will be degraded to 20 meters while holding the range resolution at 7 meters (typical for an LTE signal). The clutter patches are arranged in a 2×2 grid as shown in Fig. 25.

- $R_{res} = 7$ m, $CR_{res} = 20$ m
- $A_1 = 40$ m^2, $A_2 = 30$ m^2, $A_3 = 40$ m^2, $A_4 = 30$ m^2, $A_t = 15$ m^2
- $\sigma_c^2 = [4, 1, 8, 12]$, $\sigma_t^2 = 40, \sigma_n^2 = 1$
- $v = 100$ m/s, $f_{PRF} = 10000$ Hz, $R = 1000$ m, $Z = 1000$ m, $\theta = 0.02$ rad
- $\ell_R = 3$ m, $\ell_{CR} = 5$ m, $h = 1$ m

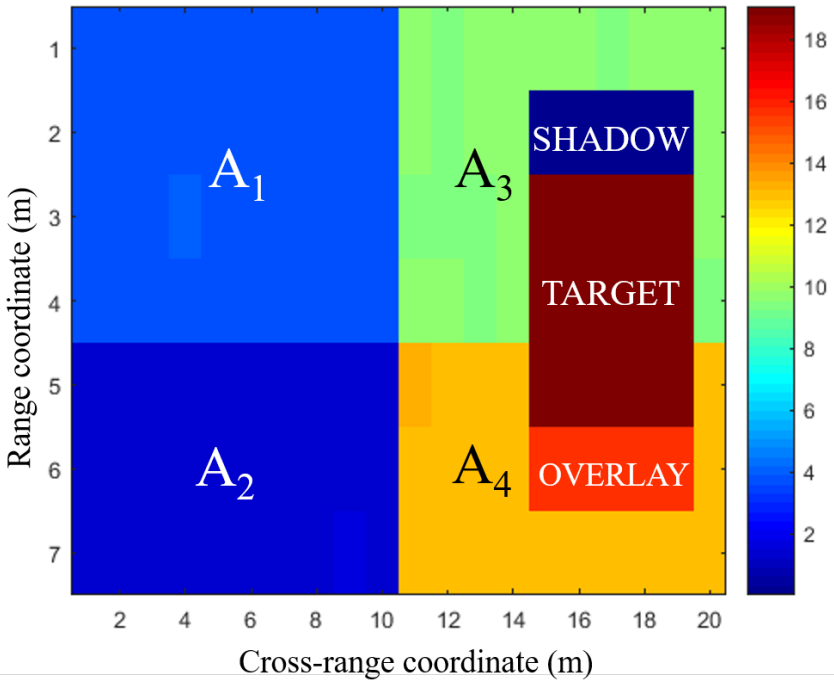

Figure 25: The experiment with 4 clutter patches is laid out in a 2x2 grid of clutter patches with a 3 m x 5 m target.

4.3.2 Deriving Hypothesis PDFs.

In the detection test, the same two hypotheses still hold:

$$H_0 : |S_r| \sim \text{Rayleigh}(\sigma_0)$$
$$H_1 : |S_r| \sim \text{Rayleigh}(\sigma_1) \tag{64}$$

The calculation for σ_0^2 is not reliant upon the position of the target and is therefore straightforward to calculate.

$$\begin{aligned}\sigma_0^2 &= A_1^2\sigma_{c1}^2 + A_2^2\sigma_{c2}^2 + A_3^2\sigma_{c3}^2 + A_4^2\sigma_{c4}^2 + \left(\sum_{k=1}^{K} A\right)\sigma_n^2 \\ &= (1600)(4) + (900)(1) + (1600)(8) + (900)(12) + (140)(1) \\ &= 31040 \end{aligned} \tag{65}$$

Adhering to the same criteria as the previous simulation (target corners fall on lattice points and are entirely within the resolution cell), there are 80 possible positions for the target. Because of the shadow and overlay, nearly all of these will have a different σ_1^2 value, and it is necessary to again define the prior probability for σ_1^2. Based upon a one-way radar range of 1000 m and a platform altitude of 1000 m, there is a 45° grazing angle. Given a target height of 1 meter, there is a shadow 1 meter in length with the width of the target and a 1 meter overlay due to the height of the target. The area of the overlay is denoted as A_{ov} and has the same scattering characteristics as the target. This layout can be seen in Fig. 25. Table 6 shows the σ_1^2 values at each target position, which are calculated as

$$\begin{aligned}\sigma_1^2 &= (A_1 - \epsilon_1)^2\sigma_{c1}^2 + (A_2 - \epsilon_2)^2\sigma_{c2}^2 + (A_3 - \epsilon_3)^2\sigma_{c3}^2 \\ &\quad + (A_4 - \epsilon_4)^2\sigma_{c4}^2 + (A_t + A_{ov})^2\sigma_t^2 + \left(\sum_{k=1}^{K} A\right)\sigma_n^2 \\ &= 4(40 - \epsilon_1)^2 + 1(30 - \epsilon_2)^2 + 8(40 - \epsilon_3)^2 \\ &\quad + 12(30 - \epsilon_4)^2 + 40(15 + A_{ov})^2 + (140)(1) \end{aligned} \tag{66}$$

Table 6: Calculation of σ_1^2 for 4 Rayleigh clutter types where the coordinates column represents the range of coordinates for which the appropriate A and $\boldsymbol{\epsilon}$ values apply. The area of the target is 15 m^2, but some positions include an additional 5 m^2 of overlay in the σ_1^2 calculation. The top row entry ($A_t = 0$) represents σ_0.

coordinates		ϵ_1	ϵ_2	ϵ_3	ϵ_4	A_{ov}	A_s	σ_1^2
-	-	0	0	0	0	0	0	31040
(1,1)	(1,6)	15	0	0	0	5	0	43140
(2,1)	(2,6)	20	0	0	0	5	5	42240
(3,1)	(3,6)	15	5	0	0	5	5	42865
(4,1)	(4,6)	10	10	0	0	5	5	43740
(5,1)	(5,6)	5	15	0	0	0	5	37865
(1,11)	(1,16)	0	0	15	0	5	0	39240
(2,11)	(2,16)	0	0	20	0	5	5	37440
(3,11)	(3,16)	0	0	15	5	5	5	35940
(4,11)	(4,16)	0	0	10	10	5	5	35440
(5,11)	(5,16)	0	0	5	15	0	5	28940
(1,7)	(1,7)	12	0	3	0	5	0	41928
(1,8)	(1,8)	9	0	6	0	5	0	40932
(1,9)	(1,9)	6	0	9	0	5	0	40152
(1,10)	(1,10)	3	0	12	0	5	0	39588
(2,7)	(2,7)	16	0	4	0	5	5	40512
(2,8)	(2,8)	12	0	8	0	5	5	39168
(2,9)	(2,9)	8	0	12	0	5	5	38208
(2,10)	(2,10)	4	0	16	0	5	5	37632
(3,7)	(3,7)	12	4	3	1	5	5	40996
(3,8)	(3,8)	9	3	6	2	5	5	39369
(3,9)	(3,9)	6	2	9	3	5	5	37984
(3,10)	(3,10)	3	1	12	4	5	5	36841
(4,7)	(4,7)	8	8	2	2	5	5	41680
(4,8)	(4,8)	6	6	4	4	5	5	39820
(4,9)	(4,9)	4	4	6	6	5	5	38160
(4,10)	(4,10)	2	2	8	8	5	5	36700
(5,7)	(5,7)	4	12	1	3	0	5	35564
(5,8)	(5,8)	3	9	2	6	0	5	33521
(5,9)	(5,9)	2	6	3	9	0	5	31736
(5,10)	(5,10)	1	3	4	12	0	5	30209

All target locations include a shadow except the range coordinate where the shadow extends into the neighboring resolution cell. Likewise, the target overlay, which occurs due to the height of the target being nearer in range to the receiver than the base of the target, occurs in each range coordinate except where the overlay is in the nearer resolution cell in range.

Even with a target which is substantially more reflective than the clutter background, there still exist target locations for which $\sigma_1^2 < \sigma_0^2$ due to the shadowing and replacement of highly-reflective clutter. Table 6 shows the extreme degree of model mismatch which can occur if the specific segment of replaced clutter is not considered. The smallest value for σ_1^2 is 28940 and the largest is 43740, which is over 50% larger; the position of the target within the resolution cell strongly influences the statistics of the signal and clutter return.

The PDF for the test statistic is derived in a similar manner as Section 4.1. Since the zero-mean assumption still holds for each the I and Q portions of the return, the only necessary calculation is the variance, which has already been determined. The PDF for σ_0^2 is a χ^2 distribution and the PDF for σ_1^2 is a sum of properly scaled PDFs based on the prior distribution of the target location. Fig. 26 shows the individual PDFs for each target location against the PDF for σ_0, while Fig. 27(a) shows the sum of the target-present PDFs against the target-absent PDF, along with the threshold that maximizes decision accuracy.

For this particular case, there are values of σ_1^2 that are less than σ_0^2, but due to the low probability of those σ_1^2 values occurring, there is not a lower threshold to identify those target positions. The resultant ROC curve is shown in Fig. 28.

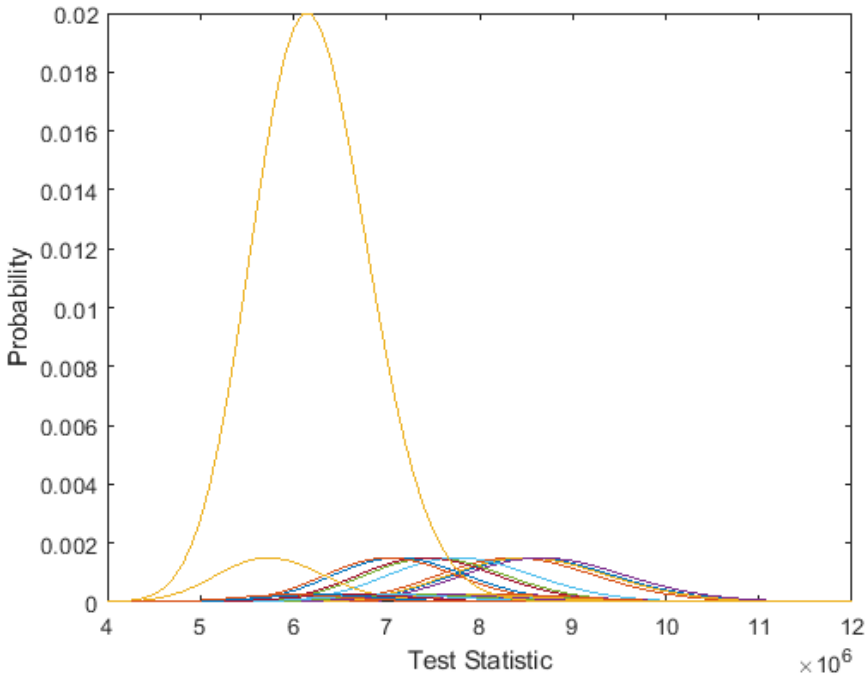

Figure 26: Probability distribution functions for target-absent (large PDF, yellow) and target-present scenarios, colored by hypothesis target location.

4.3.3 Model Mismatch.

Fig. 27 showcases one of the challenges in detection with heterogeneous clutter; because of the unknown target position, the overall PDF for a target-present scenario widens when there is uncertainty as to which clutter sections are obstructed by the target. Fig. 27(b) shows how the PDFs and ROC curve would result if the traditional set of SAR detection hypotheses, as described in Eq. (1) are used instead of the clutter replacement model as described in Eq. (2). Fig. 29 shows the difference between the two ROC curves. The area between the two curves demonstrates that a detector which does not consider the location of a target over-estimates its performance. Using a clutter replacement model provides a more modest assessment of the detector capability.

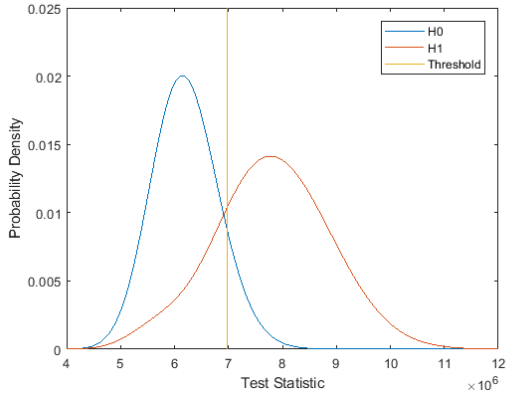

(a) Probability distribution functions for H_0 and H_1 along with ideal threshold. The H_1 PDF is stretched more than H_0 because it is comprised of many χ_2 functions with wide-ranging parameters.

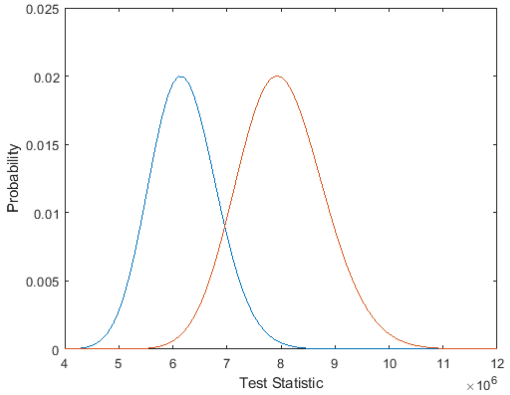

(b) The PDFs for a detection model which does not consider clutter replacement - the PDF for H_1 is a similar shape to H_0 because the location of the target is not relevant in this scenario.

Figure 27: This figure illustrates the difference in target-present PDFs using the clutter replacement model (a) as opposed to the clutter addition model (b).

4.3.4 Verification of Results.

Once again, a simulation was performed to verify that the detector is capable of achieving the detection and false alarm rates indicated by the ROC curve. Using the thresholds which maximize the accuracy rate ($\frac{P_d+(1-P_{fa}}{2}$), the theoretical values of (P_{fa}, P_d) are (0.1095, 0.7448). After a simulation with 10,000 trials, the detector performed at false-alarm and detection rates of (0.1162, 0.7467). Based on the binomial test, these values are within the 95% confidence interval for simulated results, validating the ROC curves.

4.3.5 Position Estimation.

4.3.5.1 Cost Matrix.

The dimension of the cost matrix is 30×30 since there are 30 target positions (out of 80 total) which yield distinct $\boldsymbol{\epsilon}$ values. To simplify, this can be reduced to a 10×10 cost matrix where the $\boldsymbol{\epsilon}$ values of lower prior probability are neglected. Each

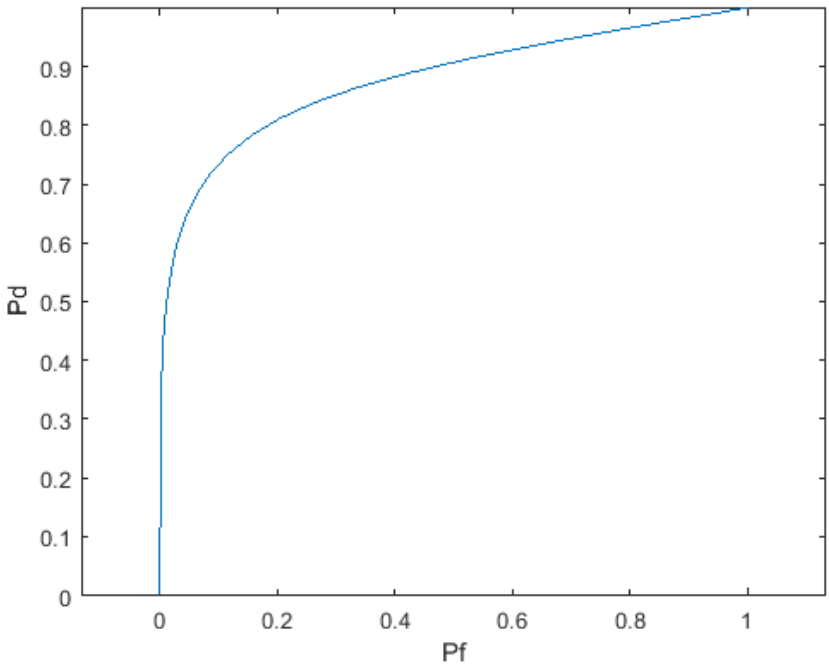

Figure 28: Probability of detection compared to probability of false alarm for a resolution cell with 4 clutter patches. There is a sharp bend in the ROC curve since the target-absent PDF is much narrower than the target-present PDF.

of the 10 remaining $\boldsymbol{\epsilon}$ values encompasses six target locations, so the reduced 10×10 cost matrix still accounts for 3/4 of possible target locations (60/80) and is 1/9 the size of the 30×30 matrix. Eq. (67) shows the cost matrix under these conditions.

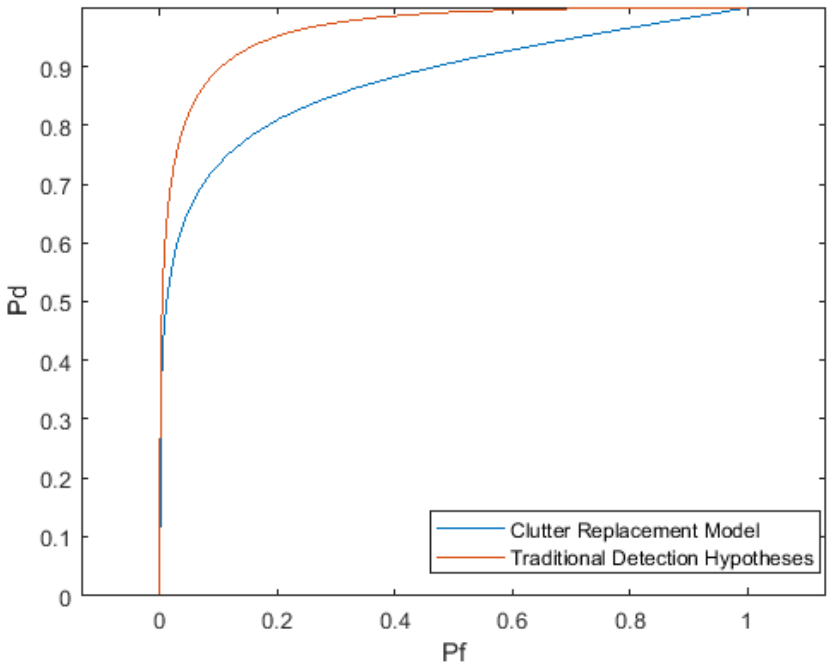

Figure 29: The two ROC curves show the model mismatch between reality (clutter replacement model) and a traditional detection hypothesis (target return supplements clutter and noise).

$$C = \begin{bmatrix} 1.50 & 1.87 & 2.59 & 3.43 & 4.34 & 10.00 & 10.05 & 10.20 & 10.45 & 10.79 \\ 1.87 & 1.50 & 1.87 & 2.59 & 3.43 & 10.05 & 10.00 & 10.05 & 10.20 & 10.45 \\ 2.59 & 1.87 & 1.50 & 1.87 & 2.59 & 10.20 & 10.05 & 10.00 & 10.05 & 10.20 \\ 3.43 & 2.59 & 1.87 & 1.50 & 1.87 & 10.45 & 10.20 & 10.05 & 10.00 & 10.05 \\ 4.34 & 3.43 & 2.59 & 1.87 & 1.50 & 10.79 & 10.45 & 10.20 & 10.05 & 10.00 \\ 10.00 & 10.05 & 10.20 & 10.45 & 10.79 & 1.50 & 1.87 & 2.59 & 3.43 & 4.34 \\ 10.05 & 10.00 & 10.05 & 10.20 & 10.45 & 1.87 & 1.50 & 1.87 & 2.59 & 3.43 \\ 10.20 & 10.05 & 10.00 & 10.05 & 10.20 & 2.59 & 1.87 & 1.50 & 1.87 & 2.59 \\ 10.45 & 10.20 & 10.05 & 10.00 & 10.05 & 3.43 & 2.59 & 1.87 & 1.50 & 1.87 \\ 10.79 & 10.45 & 10.20 & 10.05 & 10.00 & 4.34 & 3.43 & 2.59 & 1.87 & 1.50 \end{bmatrix} \tag{67}$$

4.3.5.2 Risk Calculation.

The thresholds for each section are selected in order to minimize the total risk. The total risk is another expression for the expected absolute error when making a decision. There are 10 possible hypotheses, so 9 thresholds need to be determined. Because there are so many potential combinations for thresholds, an efficient way to select the thresholds is to create a random bank of thresholds, calculate the risk, then repeat for a large number of banks and find which set minimizes the risk. In this case, 20000 sets of 9 thresholds were tested.

Fig. 30 shows the thresholds compared to the PDFs for each segment that was considered. These thresholds yield a risk of 4.09 meters. The average error that would occur if the center of the resolution cell was the estimated position is 5.31 meters. This method of multiple hypothesis detection reduces the target position estimation error by approximately 23%.

4.3.5.3 Simulation.

A simulation of 1,000 Monte Carlo trials was conducted to determine the average absolute position error of a target amongst 4 Rayleigh clutter sections using the decision methodology outlined previously. In this simulation, the target position is uniformly distributed across the resolution cell, with the stipulation that the entire target is within the cell. This simulation yields an average absolute error of 4.21 meters.

The discrepancy between the simulated error and the theoretical error is attributable to the fact that the theoretical case only considered $\boldsymbol{\epsilon}$ values with high prior probabilities in order to reduce the size of the cost matrix. This tactic reduces the cost matrix to 1/9 of its original size while covering 3/4 of the possible locations, but the remaining 1/4 of positions will be estimated at a larger error because

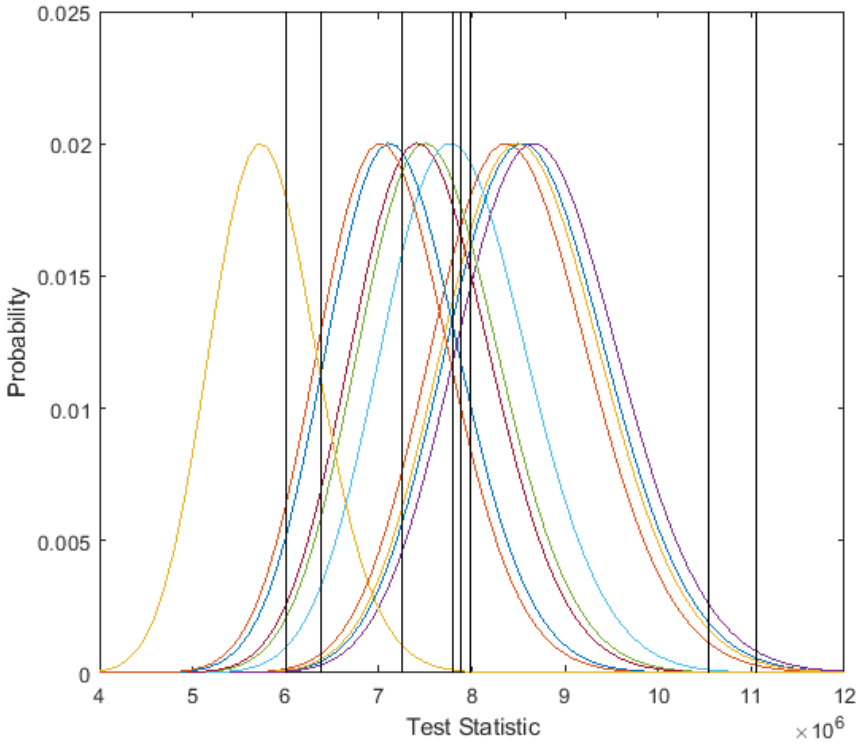

Figure 30: Nine thresholds (2 are too close together to be discerned) determine the decision regions for 10 of the possible locations of the target, whose PDFs are represented. The colors of the PDFs only serve to differentiate the PDFs from one another and have no significance.

there is no detection decision which can estimate their positions accurately. A major reduction in the volume of data processing necessary amounts to an additional 3% estimation error.

The simulation was run once again, this time only randomly placing the targets in the locations defined by the cost matrix. Again using 1,000 trials, the average absolute error is 4.06 meters, which is very close to the theoretical outcome.

V. Conclusion

5.1 Conclusions

The primary subject of this thesis is the characterization of the heterogeneous clutter that often arises from larger SAR resolution cells. This study of the effect of heterogeneous clutter addresses two issues associated with low-resolution radar: target detection and target position estimation.

The target detection model developed in this thesis more accurately defines the detection capability of a radar than would a traditional detection model. Model mismatch is substantially reduced by implementing a clutter-replacement model, in which the area of clutter reflecting signal back to the radar is reduced on account of the target blocking the path of reflection from some area on the ground. The ROC curves developed to represent the true model were validated by matching theoretical results, derived from probability distributions, with experimental results from MATLAB simulations which yielded equivalent detection and false-alarm rates. The parameters were individually modified to demonstrate their effects on the ROC curve.

Refinement of the target position estimate within the resolution cell was achieved by leveraging the clutter heterogeneity to represent different PDFs for the radar return at target positions where the target obstructs different types and amounts of clutter. The estimation was performed as a multiple hypothesis detection test where each hypothesis represents a different target position. The measure of success is the reduction in average absolute error between the estimate and the true target location, compared to the baseline error value that arises from always predicting the target to be at the center of the resolution cell.

Several other noteworthy conclusions which can be drawn from the results of this research include:

- The Rayleigh-magnitude SIRV clutter model provides a χ^2-distributed test statistic for the radar return from a resolution cell with heterogeneous clutter.

- In a detection test with non-contiguous decision regions, a set of pairs of thresholds must be tested to generate the ROC curve. In a multiple hypothesis detection test with Y decision regions, a bank of groups of $(Y-1)$ thresholds must be tested to minimize the risk function.

- Targets that are more highly-reflective are not necessarily more likely to be detected, depending on the background clutter characteristics. Also, the target positioning error generally increases with the reflectivity of a target. Heterogeneous clutter and distinct clutter types allow for position estimation within a resolution cell; as the target reflectivity increases, the relative difference among clutter patch reflectivities diminishes.

- An increase in the number of sub-aperture images utilized (data availability) improves detection performance, assuming that the condition of independent sub-apertures is met.

- The cost matrix is an effective tool in determining the thresholds and decision regions for discrete target position estimation which minimizes positioning error.

These conclusions were drawn based upon the selected examples within this thesis and require additional study to generalize.

5.2 Future Work

This thesis has set a baseline for detecting targets within low-resolution, heterogeneous clutter cells. There are several key assumptions and parameters that must be validated in order to extend the work completed in this research.

5.2.1 Independence of SAR Sub-aperture Images.

One of the key assumptions underlying the detection and position estimation experiments in this thesis is the independence of the sub-aperture data. With this assumption, there is no limit to the number of 2-pulse sub-apertures that can be collected over a given support angle. This thesis did not consider the constraints that must be implemented to avoid losing independence (sub-apertures are spaced too close together and are highly correlated) or the identical distribution (sub-apertures are spaced too far apart and the clutter and target have different distributions at different azimuth angles). Further study will be required to determine the minimum angular spacing between sub-apertures to ensure independent, identically-distributed images.

5.2.2 Bistatic Scenarios.

Passive bistatic sensing is an emerging area of study, and low-resolution target detection is an important component to its successful implementation. Bistatic scenarios for heterogeneous clutter should yield better detection and estimation performance than monostatic scenarios due to exacerbated shadow profiles.

5.2.3 Cost Matrix Adjustments.

In this thesis, the cost matrix was developed by assigning coordinates to an estimated position which minimize error for a correct decision. The cost matrix should be experimented upon to attempt to further minimize location error. Better results may arise if the cost of an incorrect decision is reduced, at the expense of the cost of a correct decision.

5.2.4 Verifying Clutter Models.

One of the primary assumptions of this research is that the clutter of interest can be modeled as a complex SIRV with Weibull-distributed magnitude; it is also assumed that the individual pulse returns from each clutter patch are independent and identically distributed. It is necessary to take physical measurements of the materials which could potentially comprise the clutter in a real-world scenario to verify that this is the case, and to use these values to conduct the detection and estimation tests.

5.2.5 Leveraging Multiple Look-Angles.

The identical distribution component of the i.i.d. assumption for clutter is based upon the fact that the SAR azimuth support is small enough that all of the collected pulses come from a virtually identical look-angle. It is also important to have a small azimuth support in order to consistently model the effects of the shadow and 3-D overlay. One of the drawbacks to the limited support is the scarcity of collected data.

A workaround to this trade-off is to repeat the search at a different look-angle. This may result in different distributions for the clutter patches or the target, and would be a separate detection and estimation problem if the parameters for H_0 and H_1 are significantly different. By integrating the results from these separate searches together, it is conceivable to create a likelihood function for the position of the target at each look-angle, then compare across searches to determine the overall most-likely position for the target.

Fig. 31 illustrates the difference in parameters which arises from varying the look-angle.

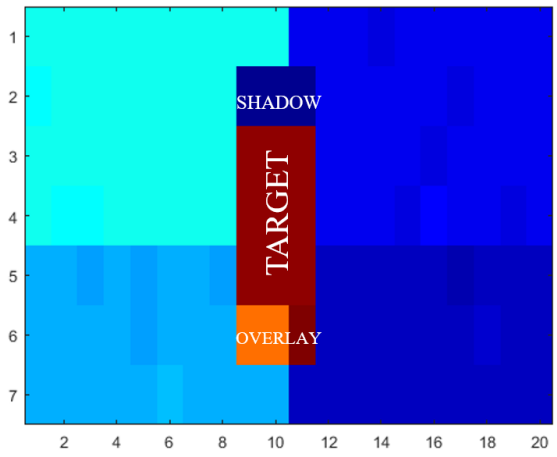

(a) Aircraft is collecting from bottom edge of scene, casting a shadow and target overlay in the range dimension

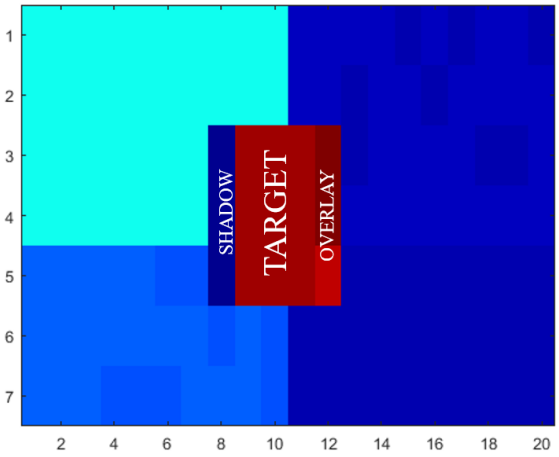

(b) Aircraft is collecting from right edge of scene, casting a shadow and target overlay in the cross-range dimension

Figure 31: The scattering statistics of the resolution cell change when a different look-angle is used due to the shadow of the target.

5.2.6 Non-Rayleigh Clutter.

All of the clutter models considered in this thesis are Rayleigh-distributed in magnitude; the Rayleigh distribution is a special case of the Weibull distribution ($b = 2$) where the I and Q components are normally distributed and can form a test statistic with a known (χ^2) distribution that can be expressed in a closed form. As discussed in Chapter 2, the process used to combine the Rayleigh scatterers into a χ^2 test statistic cannot be applied for Weibull distributions with other b parameters. If it is determined that the clutter distribution models of interest are non-Rayleigh, Weibull-distributed in magnitude, then the methodology for determining the decision regions can be modified by replacing the χ^2 distribution with whatever distribution arises from combining the random variables involved in the new model.

5.2.7 Resolving Complex Weibull Sums.

The challenge of deriving a closed form for the sum of real-valued Weibull-distributed random variables is an enormous task, in and of itself. The results from this thesis lean on the ability to utilize the Rayleigh variant of the Weibull distribution to express detection methodologies and probabilities in a closed form. The matter of solving sums of complex Weibull random variables, as opposed to real-valued, adds another layer of complexity to this problem. Research into developing a methodology for summing Weibull-distributed random variables would be a suitable follow-on to this thesis.

Bibliography

1. S. Gabert, J. A. Jackson, and R. Kappedal, "Estimating PDFs in heterogeneous radar clutter," in *2016 USNC-URSI Radio Science Meeting - Proceedings*, (Fajardo, Puerto Rico), pp. 97–98, July 2016.

2. D. Casasent and R. Shenoy, "Synthetic aperture radar detection and clutter rejection minace filters," *Pattern Recognition*, vol. 30, pp. 151–161, January 1997.

3. R. Goodman and W. Carrara, "Synthetic Aperture Radar Algorithms," in *Handbook of Image and Video Processing* (A. Bovik, ed.), pp. 1131–1153, San Diego, CA: Elsevier Academic Press, 2005.

4. A. Moccia and A. Renga, "Bistatic synthetic aperture radar," in *Distributed Space Missions for Earth System Monitoring*, pp. 3–59, New York, NY: Springer, 2013.

5. J. A. Jackson, "Model Mismatch Effect in Coarse Resolution Heterogeneous Clutter Cells," in *2019 IEEE Radar Conference*, (Boston, MA), pp. 1–6, April 2019.

6. K. El-Darymli, P. McGuire, D. Power, and C. Moloney, "Target detection in synthetic aperture radar imagery: a state-of-the-art survey," *Journal of Applied Remote Sensing*, vol. 7, pp. 1–35, March 2013.

7. R. O. Harger, "Synthetic Aperture Radar Fundamentals and Image Processing," *SAR Fundamentals and Image Processing*, vol. 2, pp. 269–286, January 1993.

8. S. Sayama and H. Sekine, "Weibull, log-Weibull and K-distributed ground clutter modeling analyzed by AIC," *IEEE Transactions on Aerospace and Electronic Systems*, vol. 37, pp. 1108–1113, July 2001.

9. G. W. Stimson, *Introduction to Airborne Radar, Third Edition*. Raleigh, NC: SciTech Publishing, Inc., 2013.

10. A. Evers and J. A. Jackson, "Experimental passive sar imaging exploiting lte, dvb, and dab signals," in *2014 IEEE Radar Conference*, (Cincinnati, OH), pp. 0680–0685, May 2014.

11. H.-J. Li and Y.-W. Kiang, "Radar and inverse scattering," in *The Electrical Engineering Handbook* (W. K. Chen, ed.), pp. 671 – 690, Burlington, MA: Academic Press, 2005.

12. A. Evers and J. A. Jackson, "Analysis of an LTE waveform for radar applications," in *IEEE National Radar Conference*, (Cincinnati, OH), pp. 0200–0205, May 2014.

13. L. A. Gorham and L. J. Moore, "SAR image formation toolbox for MATLAB," in *Algorithms for Synthetic Aperture Radar Imagery XVII*, vol. 7699, (Orlando, FL), pp. 1–13, April 2010.

14. H. L. Van Trees, *Detection, Estimation, and Modulation Theory, Part I*. Hoboken, NJ: John Wiley and Sons, Inc., 2003.

15. P. KaewTraKulPong and R. Bowden, "An Improved Adaptive Background Mixture Model for Real-time Tracking with Shadow Detection," in *Video-Based Surveillance Systems*, pp. 135–144, Boston, MA: Springer, 2011.

16. M. Jahangir, "Detecting Moving Targets in SAR Imagery Through Shadow Tracking," *Proceedings of EUSAR*, pp. 1–4, May 2006.

17. M. Jahangir, D. Blacknell, C. P. Moate, and R. D. Hill, "Extracting information from shadows in SAR imagery," in *International Conference on Machine Vision*, pp. 107–112, December 2007.

18. L. Bombrun, G. Vasile, M. Gay, and F. Totir, "Hierarchical segmentation of polarimetric SAR images using heterogeneous clutter models," *IEEE Transactions on Geoscience and Remote Sensing*, vol. 49, pp. 726–737, September 2011.

19. C. Y. Chong, F. Pascal, J. P. Ovarlez, and M. Lesturgie, "MIMO radar detection in non-Gaussian and heterogeneous clutter," *IEEE Journal on Selected Topics in Signal Processing*, vol. 4, pp. 115–126, January 2010.

20. E. E. Kuruoglu and J. Zerubia, "Modeling SAR images with a generalization of the Rayleigh distribution," *IEEE Transactions on Image Processing*, vol. 13, pp. 527–533, April 2004.

21. E. Conte, A. De Maio, and C. Galdi, "Statistical analysis of real clutter at different range resolutions," *IEEE Transactions on Aerospace and Electronic Systems*, vol. 138, pp. 121–130, April 2004.

22. D. A. Shnidman, "Generalized radar clutter model," *IEEE Transactions on Aerospace and Electronic Systems*, vol. 35, pp. 857–865, July 1999.

23. K. J. Sangston and K. R. Gerlach, "Coherent Detection of Radar Targets in a Non-Gaussian Background," *IEEE Transactions on Aerospace and Electronic Systems*, vol. 30, pp. 330–340, April 1994.

24. E. P. Blasch and M. Hensel, "Fusion of Distributions for Radar Clutter Modeling," *IEEE Intl Conf Information Fusion*, pp. 629–636, April 2004.

25. S. Nadarajah, "A review of results on sums of random variables," *Acta Applicandae Mathematicae*, vol. 103, pp. 131–140, September 2008.

26. P. G. Moschopoulos, "The distribution of the sum of independent gamma random variables," *Annals of the Institute of Statistical Mathematics*, vol. 37, pp. 541–544, December 1985.

27. J. A. Jackson, B. D. Rigling, and R. L. Moses, "Parametric scattering models for bistatic synthetic aperture radar," in *IEEE Radar Conference*, (Rome, Italy), pp. 1–5, May 2008.

28. M. Soumekh, *Synthetic aperture radar signal processing with MATLAB algorithms*. New York, NY: John Wiley and Sons, Inc., 1999.

29. S. M. Kay, *Fundamentals of statistical signal processing: estimation theory*. Upper Saddle River, NJ: Prentice Hall PTR, 1993.

30. S. M. Kay, *Fundamentals of Statistical Signal Processing, Volume 2: Detection Theory*. Upper Saddle River, NJ: Prentice Hall PTR, 1998.

31. K. G. Russell, *Design of Experiments for Generalized Linear Models*. New York, NY: Chapman and Hall, 2019.

REPORT DOCUMENTATION PAGE

Form Approved
OMB No. 0704–0188

1. REPORT DATE *(DD–MM–YYYY)*	2. REPORT TYPE	3. DATES COVERED *(From — To)*
12–09–2019	Master's Thesis	Oct 2016 — Aug 2019

4. TITLE AND SUBTITLE

Target Detection in Heterogeneous Clutter with Low Resolution Radar

5a. CONTRACT NUMBER

5b. GRANT NUMBER

5c. PROGRAM ELEMENT NUMBER

6. AUTHOR(S)

Stankowski, Kyle G., CIV GG-12, USAF

5d. PROJECT NUMBER

5e. TASK NUMBER

5f. WORK UNIT NUMBER

7. PERFORMING ORGANIZATION NAME(S) AND ADDRESS(ES)

Air Force Institute of Technology
Graduate School of Engineering and Management (AFIT/EN)
2950 Hobson Way
WPAFB OH 45433-7765

8. PERFORMING ORGANIZATION REPORT NUMBER

AFIT-ENG-MS-19-S-011

9. SPONSORING / MONITORING AGENCY NAME(S) AND ADDRESS(ES)

Air Force Office of Scientific Research - Remote Sensing Division
Dr. Stacie Williams, Program Officer
875 North Randolph Street, Suite 325
Arlington, VA 22203-1768
COMM 703-588-8213
Email: stacie.williams.1@us.af.mil

10. SPONSOR/MONITOR'S ACRONYM(S)

AFOSR/RT

11. SPONSOR/MONITOR'S REPORT NUMBER(S)

12. DISTRIBUTION / AVAILABILITY STATEMENT

DISTRIBUTION STATEMENT A:
APPROVED FOR PUBLIC RELEASE; DISTRIBUTION UNLIMITED.

13. SUPPLEMENTARY NOTES

14. ABSTRACT

This thesis develops a framework for SAR target detection and super-resolution in low-resolution environments. The primary focus in this research is the background clutter heterogeneity that often accompanies low range and cross-range resolutions. A corrective model which accounts for clutter replacement is developed to define the detection and false alarm rates of the detector more accurately than a traditional model in which the radar return from the target supplements the existing clutter.
In a heterogeneous clutter cell, the clutter replacement model leverages the different scattering distributions among the individual clutter types to generate a probability distribution function for the areas of each clutter type which are obstructed by a target. The location of the target can be extrapolated from the clutter replacement areas, and a multiple hypothesis detection test is conducted to determine which location estimate yields the lowest average error.

15. SUBJECT TERMS

Detection theory, low resolution radar, synthetic aperture radar, clutter modeling, multiple hypothesis detection

16. SECURITY CLASSIFICATION OF:			17. LIMITATION OF ABSTRACT	18. NUMBER OF PAGES	19a. NAME OF RESPONSIBLE PERSON
a. REPORT	b. ABSTRACT	c. THIS PAGE			Dr. Julie A. Jackson, AFIT/ENG
U	U	U	UU	108	19b. TELEPHONE NUMBER *(include area code)* (937) 255-3636 x4678; julie.jackson@afit.edu